ADVANCED ENERGY MATERIALS
www.advenergymat.de

Challenges and Progress in Anode-Electrolyte Interfaces for Rechargeable Divalent Metal Batteries

Liping Wang, Sibylle Riedel, and Zhirong Zhao-Karger**

Divalent metal batteries have attracted considerable attention in scientific exploration for sustainable energy storage solutions owing to the abundant reserves of magnesium (Mg) and calcium (Ca), the competitive low redox potentials of the Mg/Mg^{2+} (–2.37 V vs SHE) and Ca/Ca^{2+} (–2.87 V vs SHE) couples, as well as the high theoretical capacities of both metal anodes. However, the development of these batteries faces fundamental challenges stemming from the limited cycling stability and efficiency of Mg/Ca metal anodes. These issues primarily originate from the sluggish electrochemical redox kinetics of the divalent metals, particularly at the anode-electrolyte interfaces. This comprehensive review provides an up-to-date overview of advancements in the field of the anode-electrolyte interface for divalent metal batteries, covering aspects ranging from its formation, morphology, and composition to their influence on the reversible electrochemical deposition of divalent metals. Recent approaches aimed at enhancing the performance of metallic Mg and Ca anodes across various electrolytes are summarized and discussed, with the goal of providing insights for the development of new strategies in future research.

1. Introduction

In a world increasingly conscious of the environmental impact of traditional energy sources, there is a growing urgency to develop clean and sustainable alternatives. While renewable energy sources like wind, solar and tidal power hold great promise, their intermittent nature underscores the need for efficient and reliable energy storage systems. While lithium-ion batteries (LIBs) represent the state-of-the-art energy storage technology, they are facing resource challenges due to the relatively low natural abundance and the geographical uneven distribution of the resources for electrode materials, especially if LIBs are used for both, e-mobility and stationary storage sectors.[1] In the quest for more accessible, cost-effective, and sustainable energy storage options, researchers have redirected their attention to post-lithium battery systems. This renewed interest is aroused by their inherent advantages, including high theoretic energy density, improved safety properties and environmental sustainability. Among the emerging new battery chemistries, divalent metal batteries have experienced a resurgence in interest over the past two decades.[2] Divalent metal ions, such as Mg^{2+} and Ca^{2+}, offer a unique advantage by providing two electrons per redox center. Therefore, batteries based on Mg and Ca hold the potential to outperform commercial LIBs in several aspects, relying on potentially safer metal anodes with a lower tendency to form dendrites and high theoretical specific capacities (≈1340 and ≈2205 mAh g^{-1}, respectively), as well as volumetric capacities (≈3833 and ≈2073 mAh mL^{-1}, respectively).[3] Moreover, metal anodes can serve a dual functionality as both an anode and a current collector, simplifying the manufacturing process and reducing production costs. These distinctive properties make divalent metal batteries an attractive and eco-friendly choice for future energy storage solutions.[4]

As early as 2000, a prototype for rechargeable Mg batteries was demonstrated.[5] Subsequently, Ca metal batteries have also garnered increasing attention.[6] Recent research efforts have made notable progress in identifying viable electrolyte formulations and demonstrating encouraging projections for prospective cell-level performance metrics. Nevertheless, significant breakthroughs are still necessary to fully unlock their potential.[7] Divalent metal batteries encounter a range of significant challenges that hinder their practical application. One of the primary concerns relates to the interfaces between the metal electrodes and the electrolyte. Given the chemically reductive nature of metal anodes, reactions between the components of electrolytes and metal surfaces are unavoidable. The compositions and properties of

L. Wang
Institute of Organic Chemistry II and Advanced Materials
Ulm University
Albert-Einstein-Allee 11, D-89081 Ulm, Germany
E-mail: liping.wang@partner.kit.edu, liping-1.wang@uni-ulm.de
S. Riedel, Z. Zhao-Karger
Helmholtz Institute Ulm (HIU) Electrochemical Energy Storage
Helmholtzstrasse 11, D-89081 Ulm, Germany
E-mail: zhirong.zhao-karger@kit.edu
Z. Zhao-Karger
Institute of Nanotechnology (INT)
Karlsruhe Institute of Technology (KIT)
Hermann-von-Helmholtz Platz 1, D-76344 Eggenstein-Leopoldshafen, Germany

The ORCID identification number(s) for the author(s) of this article can be found under https://doi.org/10.1002/aenm.202402157

DOI: 10.1002/aenm.202402157

these surface layers significantly affect the electrochemistry of the metal anodes. Unlike the typical solid electrolyte interphase (SEI) formed in LIBs, the majority of the reported naturally formed surface films on Mg or Ca in the different electrolyte solutions are ionically non-conductive. Instead of benefiting to long-term stable anode redox reactions, these interphases behave as passivation layers, impeding the electrochemical metal deposition.[8] Due to the bivalency and high desolvation energy of the divalent metal ions, the surface layers on Mg and Ca metals exhibit high interfacial resistances for both charge and ion transfer, resulting in redox reactions with large overpotential and low Coulombic efficiency as well as uneven metal deposition.[9] In particular, it has been shown that achieving reversible Ca deposition on the Ca metal anode stands as a primary obstacle in the current development of Ca metal-based battery systems.[10]

The interface between divalent metal anodes and the electrolytes plays a pivotal role in the performance and efficiency of these emerging battery technologies. The impact of interfaces on the efficiency of redox reactions depends on factors such as composition, thickness, structure, and homogeneity.[11] The SEI design principles employed in LIBs are generally not directly transferable to divalent metal batteries, primarily due to fundamental differences in their battery chemistries. Understanding and optimizing the interface will facilitate the advancement of divalent metal batteries. Through an examination of the most recent advancements, identification of existing challenges, and outlining future directions in this field, this review aims to provide a comprehensive exploration of the intricate dynamics at the metal anode-electrolyte interface in the context of divalent metal batteries, particularly focusing on Mg and Ca metal anodes. The development of the Mg/Ca electrolytes is briefly summarized and the anode-electrolyte interfaces in selected current representative Mg/Ca electrolytes with different formation mechanisms are discussed. Following this, recent endeavors to alleviate the effects of these passivation factors are outlined, including solvation structural reorganization and the development of artificial SEI via electrolyte additives.

2. Electrolyte Design and Chemistry

2.1. Advancements of Mg-Ion Electrolytes: From Complex Compositions to Single Salts

Figure 1 shows the development history of important electrolyte for Mg batteries. It was evident in the 1930s, that Grignard reagents not only could be used for versatile chemical synthesis but also had the capability for Mg electrodeposition.[12] However, due to their intrinsic nature as strong reducing agents, they cannot be utilized as electrolytes in batteries. In 1990, Gregory et al. proposed several organo-Mg compounds and Mg organoborates as electrolyte salts.[13] Aurbach et al. developed another type of Mg-organohaloaluminate salt through the reaction between Bu_2Mg and $EtAlCl_2$ in tetrahydrofuran (THF), demonstrating reversible deposition and dissolution of Mg and an electrochemical window up to 2.5 V.[5] When combined with the Chervel phase Mo_6S_8 cathode, it successfully enabled the demonstration of a prototype for rechargeable Mg batteries. In 2008, the same research group further developed a so-called all-phenyl-complex (APC) electrolyte.[14] An optimized APC electrolyte is formed by blending the Lewis base phenyl magnesium chloride (PhMgCl) and a Lewis acid $AlCl_3$, contributing to an increased electrochemical stability over 3 V.[15] The organometallic complex electrolytes mentioned above are formulated through trans-metallation reactions in which Cl is bound to Mg and organic ligands are bound to aluminum (Al), these solutions contain multiple species including $MgCl^+$, $Mg_2Cl_3^+$ as redox active species, while the ligands of Mg and Al precursors and the chemical formula of the anionic species affect the oxidation stability of the electrolytes.[16] Although these organomagnesium based electrolytes show promising electrochemical stability, their nucleophilic nature makes them incompatible with electrophilic cathodes, such as sulfur and organic cathodes.

To allow coupling with electrophilic cathodes, different kinds of non-nucleophilic electrolytes were developed. In 2000, Liebenow et al. first reported the reversible Mg deposition in the electrolyte with the non-nucleophilic Hauser base hexamethyldisilazide magnesium chloride (HMDSMgCl).[17] Later, a similar strategy to that of Aurbach was applied by incorporating $AlCl_3$ or $MgCl_2$ into the solution to optimize the electrolyte, as demonstrated by examples such as HMDSMgCl-$AlCl_3$,[18] $(HMDS)_2$Mg-$AlCl_3$,[19] and $Mg(HMDS)_2$–$4MgCl_2$.[20] Apart from amido groups, Wang et al.[21] proposed the phenol-based Mg electrolytes, such as 2-tert-butyl-4-methyl-phenolate magnesium chloride (BMPMC)-$AlCl_3$, which exhibited an oxidation stability of ≈2.6 V versus Mg/Mg^{2+}. Emily G. Nelson et al.[22] further optimized this type of electrolytes through functioning the phenol structure with electron-withdrawing fluorine substitutions, resulting in an improved oxidation stability of 3.05 V.[22] Besides, there are also other kinds of salt have been reported, including $(RSMgCl)_n$-$AlCl_3$ (R = 4-methyl-benzene, p-isopropylbenzene, 4-methoxybenzene, n = 1-2),[23] (DTBP)MgCl–$MgCl_2$ (DTBP = 2,6-di-tert-butylphenolate),[24] and inorganic magnesium aluminum chloride complex (MACC).[25] It should be noted, however, that electrolytes based on the Lewis base–acid combinations are generally formed through transmetalation reactions yielding the redox active cation consisting- of two Mg atoms bridged by three chlorine atoms. The cation is paired with a counter complex anion, such as an organo-aluminate, as shown in **Figure 2a,b**. The participation of monovalent $MgCl^+$ and $Mg_2Cl_3^+$ as charge carriers may offer faster kinetics for the cathode redox reaction and Mg deposition process. However, the corrosive nature of Cl^- limits the use of conventional metallic current collectors and other battery housing components such as aluminum and stainless steel components. In addition, the storage of $MgCl^+$ will significantly reduce the practical energy density of the cell because the weight of the consumed electrolyte salt must be taken into account. Therefore, in recent years, the research interest shifts to Cl-free single salt-based electrolytes.

Tutusaus et al. explored an alternative approach by investigating chloride-free single-salt electrolytes.[26] The attempt involved using a non-organometallic electrolyte solution comprising $Mg(BH_4)_2$ in 1,2-dimethoxyethane (DME).[26b] However, the utility of this electrolyte is constrained by its low anodic stability (1.7 V vs Mg). Ha et al. demonstrated the reversible deposition of Mg using commercially available $Mg(TFSI)_2$ when dissolved in glyme.[27] The electrolytes, however, exhibited a high overpotential of ≈2 V for Mg plating and stripping, coupled with a low Coulombic efficiency. In a follow-up study, to improve the

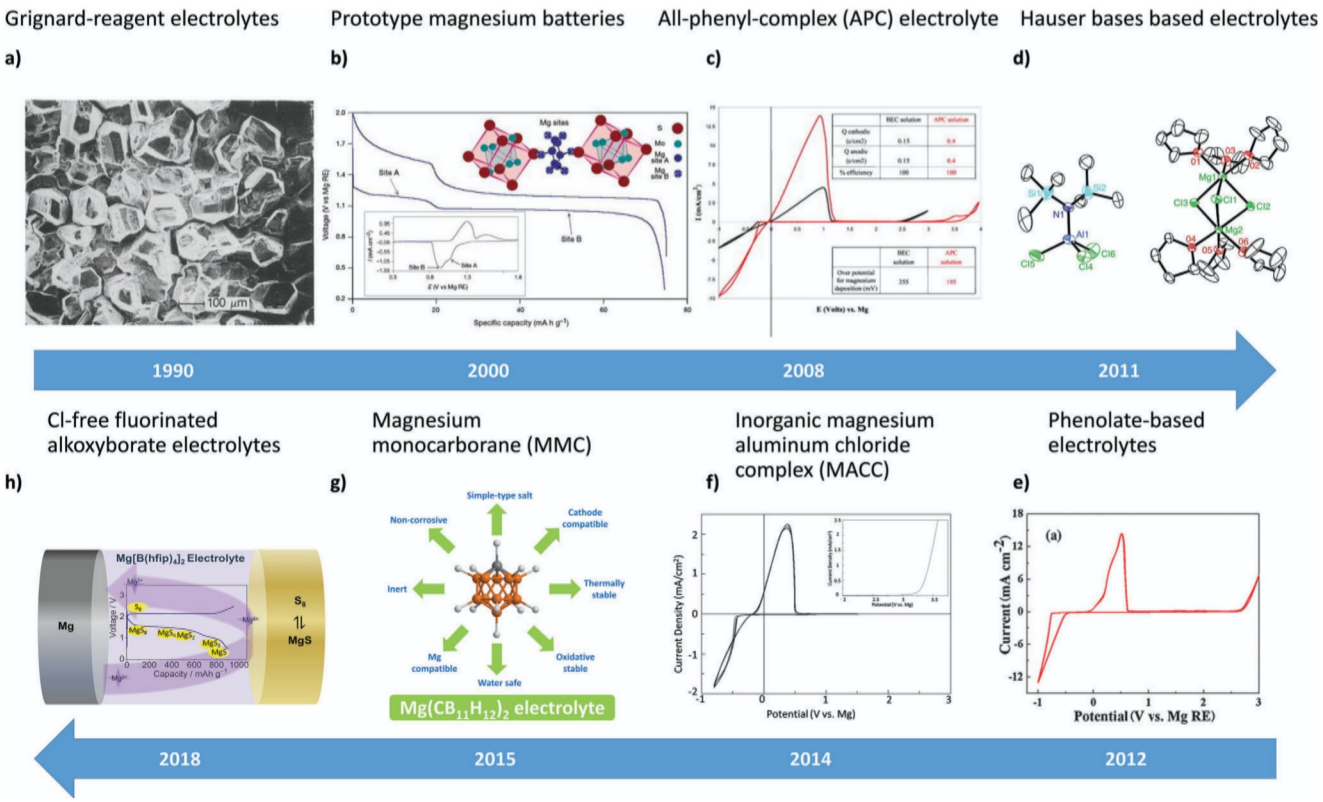

Figure 1. Timeline of the development of Mg electrolytes. a) Electronmicrograph of Mg deposit. Reproduced with permission.[13] Copyright 1990, IOP Publishing. b) The electrolyte was 0.25 M $Mg(AlCl_2BuEt)_2$ in THF. A chronopotentiogram (main figure; voltage versus capacity at constant current of 0.3 mA cm^{-2}) and a cyclic voltammogram (inset; 0.05 mV s^{-1}) of steady-state Mg insertion–deinsertion cycles are shown. Reproduced with permission.[5] Copyright 2000, Springer Nature. c) (Color online) Steady-state cyclic voltammograms of 0.25 M BEC and 0.4 M APC solutions, measured with Pt electrodes at 25 mV s^{-1}. The charge involved, Mg cycling efficiency, and overpotential for Mg deposition are given as well. Reproduced with permission.[14] Copyright 2008, IOP Publishing. d) ORTEP plot (25% thermal probability ellipsoids) of $[Mg_2Cl_3\text{-}6THF][HMDSAlCl_3]$. Hydrogen atoms, THF of crystallization, and second component of disorder are omitted for clarity. Reproduced with permission.[18] Copyright 2011, Springer Nature. e) Cyclic voltammograms (10 cycles) of Pt electrodes in $(BMPMC)_2$–$AlCl_3$/THF electrolyte exposed to air for 3 h at a scanning rate of 50 mV s^{-1}. Reproduced with permission.[21] Copyright 2012, Royal Society of Chemistry. f) Depicts the cyclic voltammogram and linear sweep voltammetry (insert) of 0.25 M MACC 2 : 1 solution in DME. The working electrode is Pt while the counter and reference electrodes are Mg metal. Measurements are obtained at 25 mV s^{-1} and ambient conditions. Reproduced with permission.[25] Copyright 2014, Royal Society of Chemistry. g) A simple yet multifaceted magnesium monocarborane (MMC) based electrolyte. Reproduced with permission.[26a] Copyright 2015, John Wiley and Sons. h) Utilizing magnesium tetrakis(hexafluoroisopropyloxy) borate $Mg[B(hfip)_4]_2$ (hfip = $OC(H)(CF_3)_2$) electrolyte for Mg–S batteries.[29]

electrochemical properties of the $Mg(TFSI)_2$ tetraglyme solution, Ma et al. introduced $Mg(BH_4)_2$ as a water scavenger into the electrolyte system.[28] While this modification notably lowered the overpotential between Mg reduction and oxidation to 0.35 V, it also came at the expense of compromising the high oxidative stability of $Mg(TFSI)_2$ due to the presence of $Mg(BH_4)_2$. In a separate study, an electrolyte based on novel $Mg(CB_{11}H_{12})_2$ salt was proposed.[26a] This electrolyte relies on a bulky monocarborane cluster as anion, weakly coordinated to Mg^{2+}, ensuring sufficient ion transport. Meanwhile, it also shows excellent reversibility for Mg electrodes and an anodic stability up to 3.8 V versus Mg, thereby allowing the use for high-voltage cathodes. Unfortunately, carborane-type electrolytes present practical usage issues due to the nontrivial synthesis and the associated high costs.

Meanwhile, new Mg compounds with another weakly coordinating anions have been developed, namely Mg tetrakis(hexafluoroisopropyloxy) borate $Mg[B(hfip)_4]_2$ (hfip = $OC(H)(CF_3)_2$) (Figure 2c),[29] alkoxyaluminate $Mg[Al(hfip)_4]_2$[30] and Mg perfluorinated pinacolatoborate $Mg[B(O_2C_2(CF_3)_4)_2]_2$.[31] With the help of highly fluorinated anion, these electrolytes exhibit high anodic stability exceeding 4 V versus Mg and chemical compatibility with various cathode materials such as oxides, sulfur and organics. The borate and aluminates analogs constructed with hexafluoroisopropanol (hfip) are the most common electrolytes in the Mg battery research for their good electrochemical properties and cost-effective synthesis from commercially available starting materials.

In addition to liquid electrolyte systems, researchers have explored and developed gel electrolytes,[32] polymer electrolytes,[33] hybrid solid electrolyte[34] and solid-state electrolytes[35] for Mg batteries. These alternatives can offer some additional benefits such as enhanced safety, with reduced risks of internal short circuits and electrolyte leakage, as well as improved mechanical durability. Some of gel and polymer electrolytes demonstrate promising electrochemical performances. In 2022, our group have demonstrated two types of $Mg[B(hfip)_4]_2$-based gel polymer

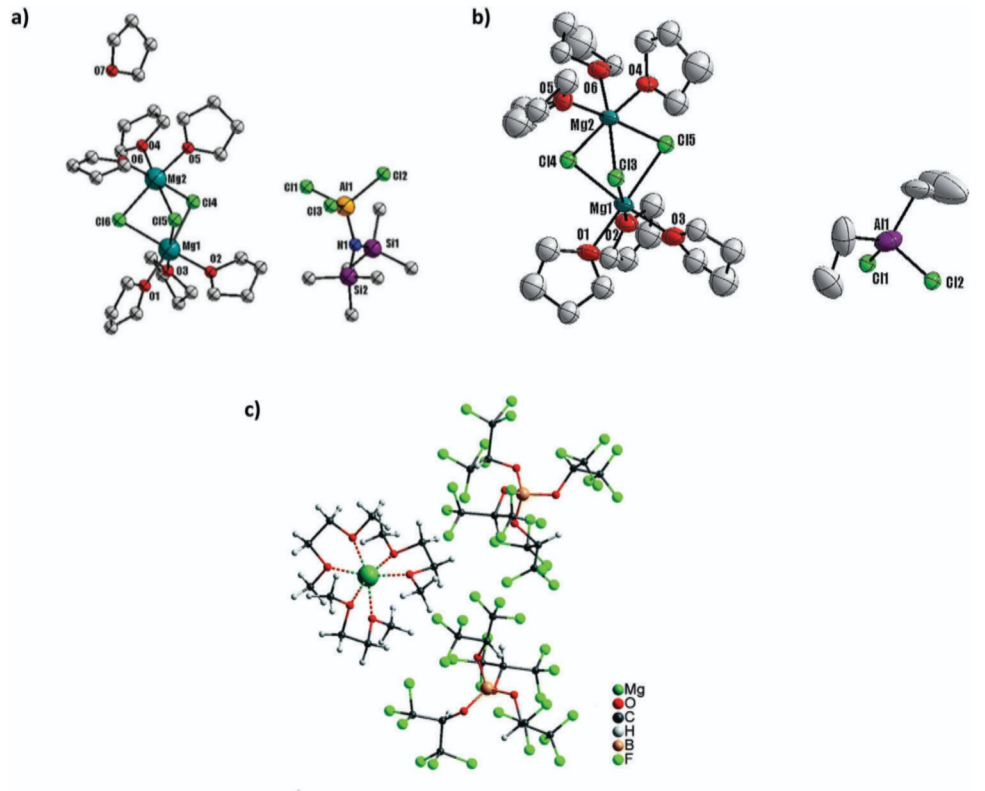

Figure 2. Single-crystal x-ray crystallographic structure of a) $[Mg_2(\mu\text{-}Cl)_3 \bullet 6THF][HMDSAlCl_3] \bullet THF$.[25c] b) $[Mg_2(\mu\text{-}Cl)_3(THF)_6][Et_2AlCl_2]$,[25c] Reproduced with permission.[25c] Copyright 2014, the Royal Society of Chemistry. c) $Mg[B(hfip)_4]_2 \bullet 3DME$.[29] Hydrogen atoms are omitted for clarity. Reproduced with permission.[29b] Copyright 2014, the Royal Society of Chemistry.

electrolyte, and applied them in Mg–S battery systems.[32f] These gel polymer electrolytes exhibited reversible Mg deposition/dissolution capabilities, along with good compatibility with sulfur cathodes. Apart from that, the polymeric matrix in the gel polymer electrolyte helps mitigate the polysulfide shuttle effect. A magnesium ion conducting hybrid solid electrolyte (HSE) was developed by Wei et al.,[34] consisting of a NASICON-structured $Mg_{0.5}Sn_2(PO_4)_3$ material, and a small amount of ionic liquid. The HSE demonstrated good compatibility with the Mg metal anode, enabling stable Mg stripping and plating at ambient temperature. Additionally, several compounds have been proposed as promising candidates as all-solid-state electrolytes, such as $MgSc_2Se_4$,[35c,d,36] and $Mg(BH_4)NH_2$.[35a,b] However, there is only limited evidence available demonstrating their feasibility in Mg full cells. Besides, developing practical solid electrolytes that conduct Mg^{2+} ions at ambient temperatures remains a significant challenge. Several representative examples of each type of electrolytes are summarized in **Table 1**, along with the corresponding electrochemical properties and test results.

2.2. Progress of Ca-Ion Electrolytes and Ca Metal Batteries

Ca possesses a lower redox potential of –2.87 V versus SHE, comparing to Mg (–2.37 V vs SHE). Furthermore, the ion radius of Ca^{2+} (1.00 Å) is larger than Mg^{2+} (0.72 Å), resulting in a lower charge-to-radius ratio and reduced polarizability. This reduced polarizability of Ca^{2+} results in milder electrostatic interactions with both the cathode material hosts and the electrolyte components, which may offer a beneficial effect on the transfer of Ca^{2+}.[4] Nonetheless, the challenges associated with the interface between the Ca metal anode and the electrolyte are equally formidable, demonstrating a complexity no less significant than that observed in the case of Mg.

The developmental trajectory of Ca metal batteries is illustrated in **Figure 3** and the corresponding electrochemical performances of some important works are summarized in **Table 2**. A pioneering research work was done by Aurbach et al. in 1991,[44] which delved into the electrochemical behavior of Ca electrodes in electrolytes of $Ca(BF_4)_2$ and $Ca(ClO_4)_2$ dissolved in propylene carbonate, γ-butyrolactone, THF or acetonitrile solvents. The study revealed that in these electrolyte systems, the deposition of Ca is quite difficult due to the specific characteristics of the surface films formed on Ca electrodes, which closely relates to the properties of the electrolyte solvent, salt, and atmospheric contaminants, similar as the case of Mg.[44] In 2003, researchers demonstrated that vanadium oxides can serve as Ca hosts, allowing for the insertion and extraction of Ca^{2+} ions with structural reversibility in $Ca(ClO_4)_2/CH_3CN$ electrolyte.[6] Ten years later, a Ca–S primary cell was reported in the same electrolyte, showing a promising discharge capacity of 600 mAh g^{-1} (calculated based on the mass of sulfur).[45] However, the full potential of the cell was hindered by the limited stability and compatibility of the electrolyte, which can form a passivation layer on

Table 1. List of Mg electrolytes and a summary of their reported electrochemical properties.

Composition	Conductivity [S cm^{-1}] at RT	Voltage window vs. Mg^0/Mg^{2+}	Coulombic efficiency	Cyclability	Refs.
0.25 M $Mg(AlCl_2BuEt)_2$ in THF	several millisiemens	≈2.5 V	≈100%	Mg–$Mg_xMo_3S_4$ cell at 0.3 mA cm^{-2}, 2000 cycles	[5]
0.4 M PhMgCl:$AlCl_3$ 2:1 in THF	$4\text{-}5 \times 10^{-3}$	>3 V	100%	Mg–Mo_6S_8 cell at C/8, 94 cycles	[14]
0.25 M MACC (3:2) in DME	2.0×10^{-3}	>3.1 V	99%	Mg–Mo_6S_8 cell at 0.5C, 15 cycles	[25a]
1.0 M HMDSMgCl in THF	0.58×10^{-3}	≈2.0 V	–	Mg–Ag/Ni, 10 cycles	[17]
0.4 M HMDSMgCl:$AlCl_3$ (3:1) in THF	/	3.2 V	100%	Mg–S cell at 50 μA g^{-1}, 2 cycles	[18]
0.35 M $[(HMDS)_2Mg]:AlCl_3$ (1:2) in G2	1.7×10^{-3}	>3.5 V	99%	Mg–Mo_6S_8 cell at 10 mA g^{-1}, 30 cycles	[19b]
1.25 M $Mg(HMDS)_2$–$4MgCl_2$	0.9×10^{-3} (60 °C, 0.75 M)	2.8 V	99%	Mg–Mo_6S_8 cell at 0.1C, 50 cycles	[20]
1.2 M $[(HMDS)_2Mg]:AlCl_3$ (1:2) in $PP_{14}TFSI$: G2/G4 (1:2)	/	>3.5 V	–	Mg–S cell at 20 mA g^{-1}, 20 cycles	[19a]
0.5 M BMPMC-$AlCl_3$ in THF	2.56×10^{-3}	2.6 V	99% (After 50 cycles)	Mg–Mo_6S_8 cell at 0.05C, 3 cycles	[21]
0.5 M $(IPBMC)_{1.5}$-$AlCl_3$ in THF	2.48×10^{-3}	2.5 V	95% to 99%	Mg–Mo_6S_8 cell at 0.38C, 100 cycles	[23]
0.5 M (DTBP)MgCl–$MgCl_2$ in THF	0.66×10^{-3}	2.3 V	100%	Mg–Mo_6S_8 cell at 0.05C, 50 cycles	[24]
0.5 M $Mg[B(Bu_2Ph_2)]_2$ in THF	1.0×10^{-3}	/	99%	0.25 M $Mg[B(Bu_2Ph_2)]_2$ in THF/DME Mg–Co_3O_4 cell at 0.87 mA, 4 cycles	[13]
0.5 M $Mg(TFSI)_2$/DME+TMP	/	>4.0 V	75-79%	Mg||Mg symmetrical cell at 0.1 mA cm^{-2}, 300 cycles	[37]
0.5 M $Mg(TFSI)_2$/DME+M4	4.0×10^{-3}	3.8 V	99.5%	Mg–$Mg_{0.15}MnO_2$ cell at 0.5C, 200 cycles	[3c]
0.4 M $Mg(TFSI)_2$ in CEPE	2.8×10^{-3}	>4.0 V	95.2%	Mg–polyaniline cell at 2C, 400 cycles	[38]
0.8 M $Mg(TFSI)_2$–$2MgCl_2$ in DME/THF	/	/	98.8%	Mg–Mo_6S_8 cell at 0.5C, 1000 cycles	[39]
$Mg(SO_3CF_3)_2$ in (DME+G_2):MOEA (5:1)	4.3×10^{-3}	3.5 V	98%	Mg–Mo_6S_8 cell at 1C, 300 cycles	[40]
0.1 M $Mg(BH_4)_2$ in DME	/	1.7 V	94%	Mg–Mo_6S_8 cell at 1C, 40 cycles (with $LiBH_4$ in electrolyte)	[26b]
0.65–0.85 M $Mg(CB_{11}H_{12})_2$ in G3/G4	2.9×10^{-3}	3.8 V	>99%	Mg–MnO_2 cell at 0.2 mA cm^{-2}, 1 cycle	[26a]
0.05 M $Mg(FCB_{11}H_{11})_2$ in G3	0.14×10^{-3}	4.6 V	>99%	/	[41]
0.5 M $Mg(CB_{11}H_{12})_2$ in DME:G2 (1:1)	6.1×10^{-3}	/	99.9%	Mg–PTO cell at 0.2C, 700 cycles	[42]
0.6 M $Mg[B(hfip)_4]_2$ in DME	6.8×10^{-3}	4.3 V	>98%	Mg–S cell at 0.1C, 100 cycles	[29b]
0.3 M $Mg[B(hfip)_4]_2$ in DME	1.1×10^{-2}	4.5 V	–	Mg–S cell at 0.1C, 100 cycles	[43]
0.5 M $Mg[B(O_2C_2(CF_3)_4)_2]_2$ (Mg-FPB) in G2	3.95×10^{-3}	>4.0 V	95%	Mg–MnO_2 cell at 10 μA g^{-1}, 1 cycle	[31]
0.3 M $Mg[Al(hfip)_4]_2$ in G2	$>5 \times 10^{-3}$	>4.0 V	99.4%	Mg–Cu cell at 0.5 mA cm^{-2}, 250 cycles	[30]
0.24 M $Mg[B(hfip)_4]_2$ in DME/PTHF	2.01×10^{-3}	2.57 V	≈99%	Mg–S cell at 0.1C, 100 cycles	[32a]
PDEGVE@GF GPE	1.24×10^{-4}	>4.0 V	99.99%	Mg–Mo_6S_8 cell at 1C, 3000 cycles at 30 °C	[32b]
PTB@GF-GPE	4.76×10^{-4}	>2.0 V	–	Mg–Mo_6S_8 cell at 0.5C, 250 cycles	[32c]
PECH-OMgCl@G3	6.24×10^{-5} at 30 °C	4.8 V	–	Mg–Mo_6S_8 cell at 0.5C, 200 cycles at 30 °C	[33a]

the surface of Ca anode. As a result, the electrochemical performance of the cell, especially the cycling stability, remained restricted. Subsequently, researchers increasingly directed their focus toward the development of suitable Ca electrolytes. In 2016, a reversible stripping/plating process was realized with $Ca(BF_4)_2$ based carbonate electrolyte at 100 °C.[46] This electrolyte demonstrated a voltage window up to 4 V, which allows the possibility of applying high voltage cathode materials. However, additional unwanted side reactions occurred at the same time, such as the formation of CaF_2. In 2017, a reversible Ca plating and stripping phenomenon was achieved at room temperature using a $Ca(BH_4)_2$/THF electrolyte.[47] This electrolyte exhibited a low polarization (≈100 mV) over more than 50 cycles, indicating impressive stability and efficiency in Ca metal deposition.

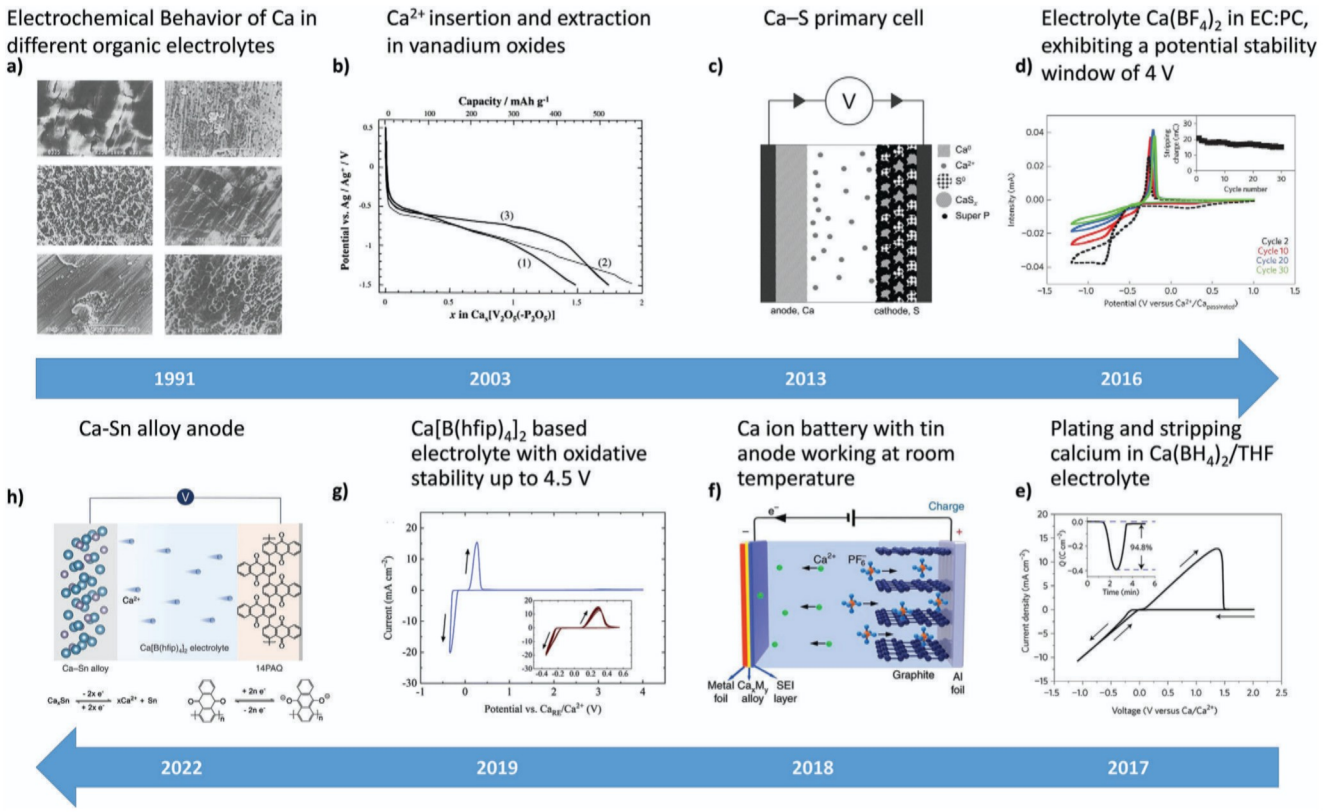

Figure 3. Timeline of the development of Ca battery technologies. a) Electrochemical behavior of Ca in different organic electrolytes. Reproduced with permission.[44] Copyright 1991, the Electrochemical Society. b) Ca^{2+} insertion and extraction in vanadium oxides. Reproduced with permission.[6] Copyright 2003, Elsevier. c) Ca–S primary cell. Reproduced with permission.[45] Copyright 2013, John Wiley and Sons. d) Electrolyte $Ca(BF_4)_2$ in EC:PC, exhibiting a potential stability window of 4 V. Reproduced with permission.[46] Copyright 2015, Springer Nature. e) Plating and stripping calcium in $Ca(BH_4)_2$/THF electrolyte. Reproduced with permission.[47] Copyright 2017, Springer Nature. f) Ca ion battery with tin anode working at room temperature. Reproduced with permission.[48] Copyright 2018, Springer Nature. g) $Ca[B(hfip)_4]_2$ (hfip = tetrakis(hexafluoroisopropyloxy)borate) based electrolyte with oxidative stability up to 4.5 V. Reproduced with permission.[49a] Copyright 2019, RSC Publishing. h) Ca-Sn alloy anode. Reproduced with permission.[50] Copyright 2022, Springer Nature.

However, similar to the $Mg(BH_4)_2$ salt-based electrolyte, the voltage window of this electrolyte is restricted to 3 V due to the reducing nature of borohydride. Soon after, efforts were made to address the anode aspect. For example, tin (Sn) metal was applied as an anode material with alloying/de-alloying reaction,[48] while anions intercalation/de-intercalation occurred simultaneously on the cathode side. This work introduced a novel dual-ion system for Ca based batteries. In 2019, a new fluorinated alkoxyborate Ca electrolyte was developed, exhibiting extended stability up to 4.5 V.[49] Additionally, this electrolyte displayed remarkable features such as high ionic conductivity and electrochemical stability, establishing a robust foundation for the feasibility of Ca batteries. The long cycling stability of full cells with this electrolyte is still limited when using the Ca metal anode due to significant passivation issues on the metal surface. Efforts to address this challenge included exploring alternative anode materials. In 2022, the feasibility of Ca-Sn alloy anodes was validated, which achieved an impressive stable charge/discharge for 5000 cycles when paired with a 1,4-polyanthraquinone organic cathode.[50] However, the produce of Ca-Sn alloy with excellent performance needs precise synthesis, while further elucidating the mechanism behind the alloying reaction is also imperative.

3. Metal Anode-Electrolyte Interface

3.1. Fundamentals of the Anode-Electrolyte Interface

As mentioned before, the component, structure as well as properties of the anode-electrolyte interface have close correlation with the battery performance. Therefore, it is crucial to first understand how this interface forms in a battery. Goodenough et al.[1a] have introduced a thermodynamic criterion for the formation of the electrode-electrolyte interface. This criterion takes into account the lowest unoccupied molecular orbital (LUMO) and the highest occupied molecular orbital (HOMO) of the electrolytes, along with the electrochemical potentials of the electrodes (μ_A for anode, μ_C for cathode). As depicted in **Figure 4a**, when the μ_A surpasses the LUMO level of the electrolyte, the electrolyte will be reduced by the anode, initiating the formation of an SEI, a focused point in this review. Similarly, if the μ_C of a cathode is lower than the HOMO of the electrolyte, redox reactions will occur unless a cathode-electrolyte interface (CEI) is established. In LIBs, the SEI forms as an intricate amalgamation of insoluble multiphase products that deposit on the anode, incorporating a diverse range of both inorganic and organic interphases.[62] An ideal SEI

Table 2. List of Ca batteries and a summary of their reported electrochemical properties.

Composition	Conductivity [S cm^{-1}] at RT	Voltage window vs. Ca^0/Ca^{2+}	Coulombic efficiency	Cyclability	Refs.
1 M $Ca(ClO_4)_2$ in CH_3CN	–	–	–	V_2O_5–Ca cell at 0.05 mA cm^{-2}, 1 cycle discharge	[6]
0.45 M $Ca(BF_4)_2$ in EC:PC	$>5 \times 10^{-3}$	4 V	–	SS–Ca cell at 100 °C, 0.2 mV s^{-1}, 30 cycles	[46]
1 M $Ca(BF_4)_2$ in EC:PC	–	≈3 V	>95%	Cu–Ca cell at 0.55 mA cm^{-2}, over 20 cycles	[51]
1.5 M $Ca(BH_4)_2$ in THF	–	≈3 V	94–96%	Au–Ca cell at 1 mA cm^{-2}, 50 cycles	[47]
1.5 M $Ca(BH_4)_2$ + 0.1 M $LiBH_4$ in THF	–	< 3 V	–	FeS_2–Ca cell at 112 mA g^{-1}, 200 cycles	[10b]
0.8 M $Ca(PF_6)_2$ in EC:PC:DMC:EMC 2:2:3:3	–	≈5 V	–	Graphite–Sn cell at 100 mA g^{-1}, 350 cycles	[48]
0.4 M $Ca(TFSI)_2$ + 2wt% BF_3•DE in EC:PC	–	–	≈30%	SS–Ca cell at 0.1 mV s^{-1}, 20 cycles	[52]
0.25 M $Ca(TFSI)_2$ in EC:DMC	–	–	–	S/CMK-3 composite–carbon cloth (AC) cell at 500 mA g^{-1}, 300 cycles	[53]
0.1 M $Ca(TFSI)_2$ in DMAc	–	–	–	$SnBr_2$-Ca–graphite cell at 100 mA g^{-1}, over 100 cycles	[54]
0.5 M $Ca(ClO_4)_2$ in CH_3CN	–	–	–	S@meso-C–Ca primary cell at C/3.5, 1 step discharge	[45]
0.25 M $Ca[B(hfip)_4]_2$ in DME	$>8 \times 10^{-3}$	4.5 V	≈80%	Ca–Ca symmetric cell at 0.2 mA cm^{-2}, 250 cycles	[49a]
0.5 M $Ca[B(hfip)_4]_2$ + 0.1 M Bu_4NCl in DME	6.7×10^{-3}	>4.1 V	92–95%	Au–Ca cell at 0.5 mA cm^{-2}, over 30 cycles	[49b]
0.25 M $Ca[B(hfip)_4]_2$ in DME (same electrolyte as referenced in[49b])	$>8 \times 10^{-3}$	4.5 V	≈80%	S/C composite–Ca cell at C/10, 15 cycles	[10c]
0.25 M $Ca[B(hfip)_4]_2$ in DME (same electrolyte as referenced in[49b])	$>8 \times 10^{-3}$	4.5 V	≈80%	1,4-polyanthraquinone–Ca-Sn alloy cell at 260 mA g^{-1}, 5000 cycles	[50]
0.25 M $Ca[B(hfip)_4]_2$ in diglyme	–	4.2 V	85.5%	$FePO_4$–Ca cell at 56 mA g^{-1}, 4 cycles	[55]
0.2 M $Ca[B(hfip)_4]_2$ in DME	–	–	≈65%	Se–Ca cell at 100 mA g^{-1}, 8 cycle	[56]
0.2 M calcium tetrakis(perfluoro-tert-butoxy) aluminate ($Ca[TPFA]_2$) in DME	–	4.5 V	55%	CuS–Ca cell at 10 mA g^{-1}, 10 cycles	[57]
0.5 M $Ca[CB_{11}H_{12}]_2$ in DME:THF	4×10^{-3}	>4 V	≈88%	Au–Ca cell at 20 mV s^{-1}, 30 cycles S–Ca cell at 167.2 mA g^{-1}, 1 cycle	[58]
0.5 M $Ca(BH_4)_2$ + 0.075 M $Ca[CB_{11}H_{12}]_2$ in THF	$\approx 2 \times 10^{-3}$	–	>93%	Ca–Ca symmetric cell at 2 mA cm^{-2}, 50 cycles	[59]
0.5 M $Ca[CB_{11}H_{12}]_2$ in DME:THF	4×10^{-3}	>4 V	≈90%	CuS/C composite–Ca cell at 1000 mA g^{-1}, over 500 cycles	[10e]
1.0 M $Ca(BF_4)_2$ in EC:PC/cross-linked PEDGA	$10^{-4} - 10^{-5}$	3.8 V	–	Ca–Ca symmetric cell at 2 μA cm^{-2}, 7 cycles	[60]
0.2 M $Ca(TFSI)_2$ in 1-ethyl-3methylimidazolium trifluoromethanesulfonate /cross-linked PEDGA	$10^{-3} - 10^{-4}$	≈4 V	–	$Ca_3Co_4O_9$–V_2O_5 at 40 μA full cell over 25 cylces	[61]

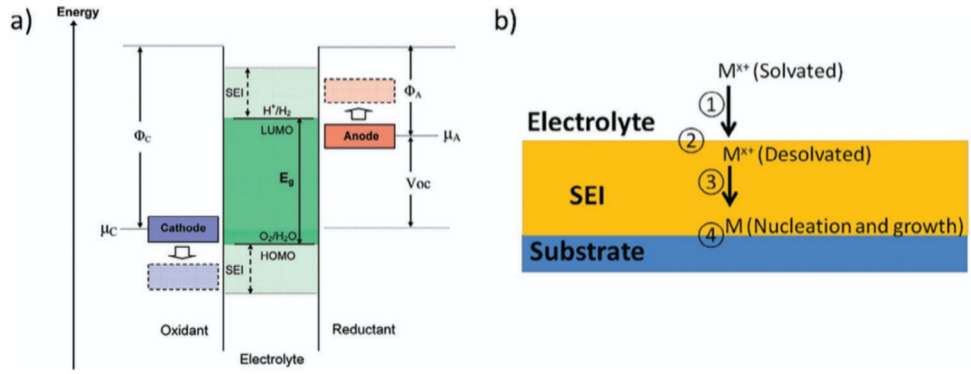

Figure 4. a) Schematic open-circuit energy diagram of an aqueous electrolyte. Φ_A and Φ_C are the anode and cathode work functions. E_g is the window of the electrolyte for thermodynamic stability. A μ_A > LUMO and/or a μ_C < HOMO requires a kinetic stability by the formation of an SEI layer. Reproduced with permission.[1a] Copyright 2010, American Chemical Society. b) Schematic representation of the four main subsequent steps involved in the global process of electrodepositing a metal on the surface of an electrode covered with a passivation layer (or Solid Electrolyte Interphase, denoted as SEI). Reproduced with permission.[46] Copyright 2015, Springer Nature.

is characterized by high ionic conductivity, appropriate thickness, and superior uniformity. However, inherent SEI is always chemically heterogeneous and mechanically fragile, lacking the capability to sustain its original composition and structure through repeated cycles. The dynamic SEI evolution during cycling results in the continuous degradation of both the anode interface and electrolyte, ultimately leading to a reduction in Coulombic efficiency and inferior cycling stability.[63] The SEI stands out as the most crucial yet least comprehended component in battery chemistry, also including divalent metal battery systems.

In divalent metal batteries, four sequential steps are involved to achieve the reversible deposition/dissolution of metal anode, as depicted in Figure 3b by Ponrouch et al.:[46] 1) solvated metal ions diffuse/migrate within the electrolyte; 2) these metal ions desolvate at the electrolyte/SEI layer; 3) the desolvated metal ions migrate through the SEI; 4) metal nucleation occurs on the anode/substrate. Evidently, SEI is intricately connected to all these four steps and plays a key role in this process.

To obtain a stable metal stripping/plating, the most important characteristic of SEI is its ability to conduct metal ions, which determines the feasibility of reversible metal deposition. Stemming from the decomposition of coordinated anions/solvents or contaminants, the majority of components within the interface of divalent metal batteries exhibit low ionic conductivity.[64] Consequently, the interlayer tends to impede the transport of divalent ions to the anode, rather than providing protection to prevent ongoing side reactions with electrolyte, as observed in LIBs.[65] Addressing these issues is crucial for achieving prolonged cycling of rechargeable divalent metal batteries. Four innovative strategies, illustrated in **Figure 5**, can help optimize the anode-electrolyte interfaces, including using electrolyte additives, tuning the M^{2+}-solvent coordination environment, modifying the interactions between M^{2+} and anions, and building artificial interphases.

In addition, the primary properties and the specific ingredients of the metal anode-electrolyte interfaces are directly determined by the composition of electrolyte. In the subsequent sections, the anode-electrolyte interfaces will be summarized and discussed, focusing on various electrolyte systems for both Mg and Ca metal batteries.

3.2. Mg Anode Interfacial Chemistries and Surface Engineering

Taking advantage of abundant nature reserves, low costs, and favorable energy density, Mg metal has emerged as a highly promising candidate for use as anode materials. While this concept holds considerable appeal, there remain significant challenges to overcome. Mg exhibits slower reaction kinetics in comparison to Li due to the higher charge density of the divalent Mg^{2+} ions (120 C mm^{-3} for Mg^{2+} vs 52 C mm^{-3} for Li^+).[2b,66] Additionally, the Mg surface strongly tends to form non-conductive interfaces from the reactive Mg with the electrolyte and moisture, as mentioned in the previous section. This section will summarize and discuss the anode-electrolyte interface in each typical type of electrolyte, covering components, metal deposition morphology, cycling stability, and other relevant aspects.

Due to intensified electrostatic interactions, desolvation and the transport of divalent ions through the SEI present more formidable obstacles, leading to significant overpotentials and reduced reversibility in the electrochemical processes.[67] Both anions and solvents can greatly impact the solvation structure of Mg^{2+} ions in the electrolyte, thereby serving as decisive factors in determining the composition of the interface. Besides, traces of oxygen, water and other organic vapors in the glove box may react with the metal anode, forming oxides and hydroxides on the surface during the process of preparing and assembling of batteries. We have selected the current representative Mg electrolytes and discussed each of them in detail separately.

3.2.1. Magnesium bis(trifluoromethanesulfonimide) ($Mg(TFSI)_2$)-Based and Magnesium Triflate ($Mg(OTf)_2$)-Based Electrolytes

$Mg(TFSI)_2$, a commercially available Mg salt, has garnered significant interest in recent years. This is primarily attributed to its notable characteristics, including good solubility in ether solvents, high ionic conductivity, and high anodic stability.[27] $Mg(SO_3CF_3)_2$ ($Mg(OTf)_2$) is also a conventional low-cost Mg salt with a smaller molecular weight, which can enhance the energy density of the batteries.[40]

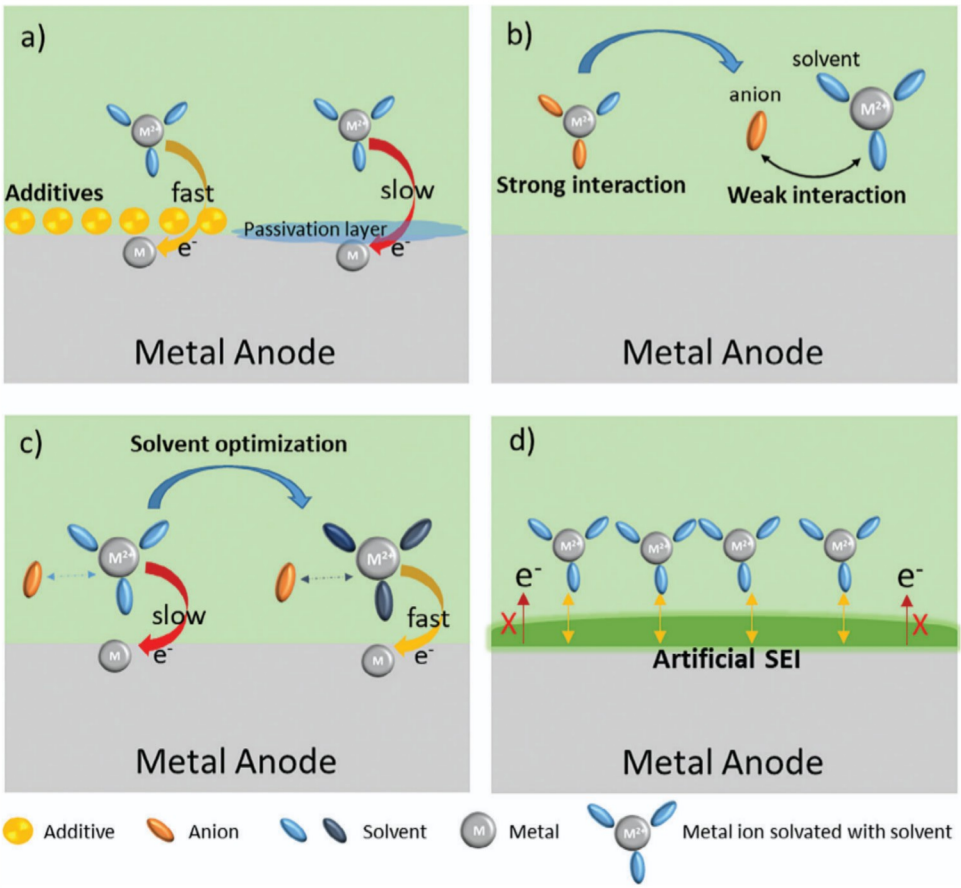

Figure 5. Four strategies to mitigate the anode-electrolyte interfacial issues in divalent metal batteries: a) Using electrolyte additives. b) Tuning the M^{2+}-anion interaction. c) Tuning the M^{2+}-solvent coordination environment. d) Building artificial interphases.

As a divalent ion, Mg^{2+} exhibits interactions that are more intricate than those of monovalent ions, playing a pivotal role in both the dissociation of Mg salts and the modulation of the coordination environment of Mg^{2+} ions. Normally, the coordination environment of Mg^{2+} ions consists of solvent and/or anion(s) depending on competing Mg^{2+}-solvent and Mg^{2+}-anion interactions. These chemical interactions are closely linked to electrochemical performance of the electrolytes and also responsible for the formation of the surface layer, since both solvents and anions can be chemically or electrochemically reduced on the metal anodes.[68] For example, within the commercially accessible $Mg(TFSI)_2$/DME electrolyte, the robust interaction makes the electron transfer from the oxygen atoms of DME to the divalent Mg^{2+}, facilitating the formation of the $[Mg(DME)_3]^{2+}$ species.[37,69] Meanwhile, the $[Mg^{2+}\text{-}TFSI^-]^+$ ion pair will also form due to the strong interaction between the cations and anions.[68b] Similarly, the commercial $Mg(OTf)_2$ salt yields the $[Mg^{2+}\text{-}OTf^-]^+$ ion pair in the electrolyte solution.[70] All these species are prone to reduction during Mg plating, decomposing into inorganic byproducts such as MgF_2/MgS for $Mg(TFSI)_2$ and $Mg(OH)_2$/MgO/MgF_2 in the case of $Mg(OTf)_2$, along with certain polymeric/organic species, leading to the formation of a substantial impedance layer on the Mg surface. This issue has been addressed from four distinct directions: incorporating salt additives like $MgCl_2$,[71] building artificial interfaces,[72] modifying anions,[73] and introducing solvent additives.[3c,37,38,40,74]

As already known, with the addition of $MgCl_2$, reversible Mg deposition with crystalline uniformity of the Mg deposits can be achieved.[71b] Sun et al.[39] improved the stability of the Mg anode by designing an electrolyte using an inorganic $Mg(TFSI)_2$–$MgCl_2$ combination in mixed DME-THF solvents. However, it has been demonstrated that the presence of chlorides in the electrolyte results in strong chemical bonding of Mg^{2+} by Cl^-, forming singly charged species $Mg_xCl_y^+$, which dominants the intercalation. As a consequence, the energy density decreases compared to divalent Mg^{2+} storage.[75] With similar concept, 1-chloropropane (CP), a covalently-bonded chloride source, was introduced into different conventional electrolytes, including $Mg(OTf)_2$, $Mg(TFSI)_2$ and $Mg(HMDS)_2$.[76] The addition of CP significantly impacts the solvation structure of these electrolytes. Through the utilization of cryo-TEM, a uniform interphase was observed on the surface of hexagonal Mg plates shown in **Figure 6**. As confirmed by EDS and XPS analysis, this interphase exhibited a Cl-rich composition, which can inhibit passivation and facilitate the electrochemical reaction kinetics. But it should be mentioned that the 5.4 vol% CP in the electrolyte corresponds to a high molar ratio of CP to $Mg(OTf)_2$, approximately three times. Furthermore, CP can also react with the Mg anode to form the Grignard compound *n*-propyl magnesium chloride,

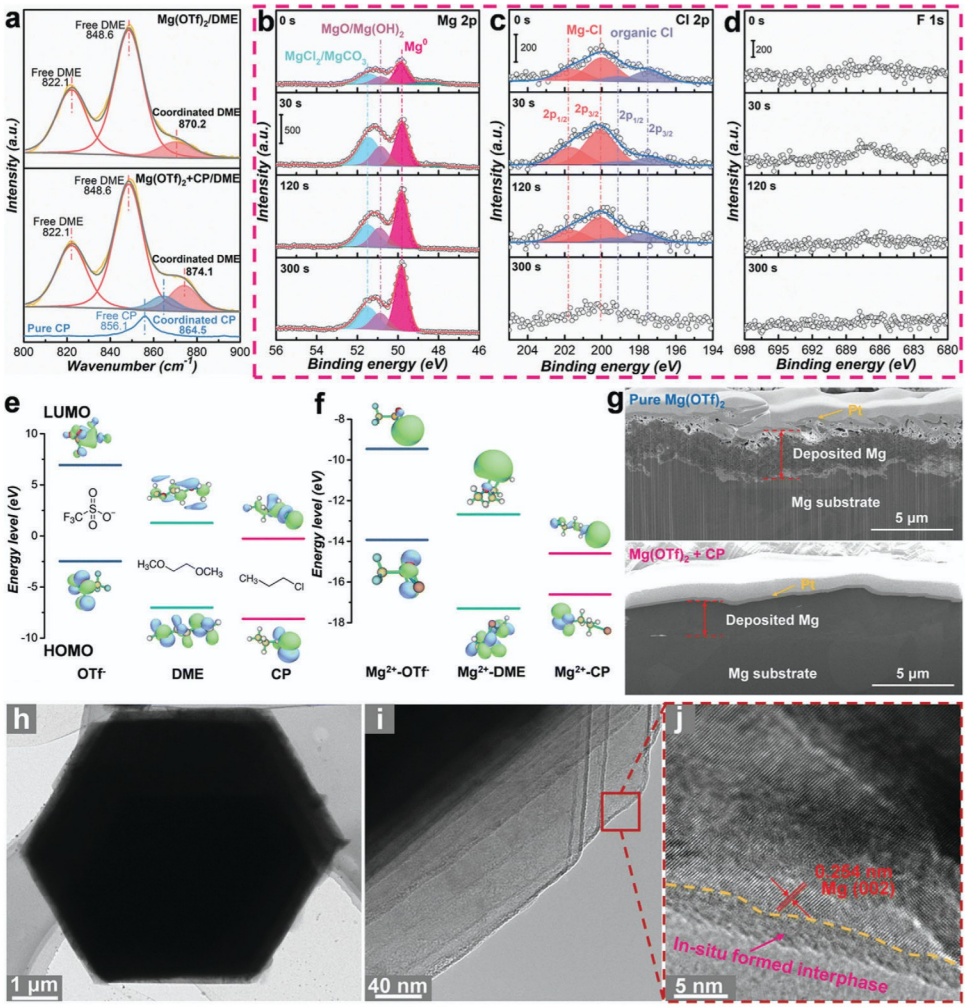

Figure 6. a) Raman spectra of $Mg(OTf)_2$/DME, CP liquid and $Mg(OTf)_2$ + CP/DME. XPS spectra of b) Mg 2p, c) Cl 2p, and d) F 1s of the cycled Mg electrode in $Mg(OTf)_2$ + CP electrolyte with different Ar etching times. The calculated LUMO and HOMO energy values of e) individual species and f) Mg^{2+} coordinated complexes in $Mg(OTf)_2$ + CP electrolyte. g) FIB-SEM cross sectional images of cycled Mg electrodes in pure $Mg(OTf)_2$ and $Mg(OTf)_2$ + CP electrolytes, respectively. The purpose of Pt deposition is to protect the electrode from ion beam damage during sample preparation. h,i) Cryo-TEM images with different magnifications and j) Cryo-HRTEM image of the surface interphase from the Mg deposit in $Mg(OTf)_2$ + CP electrolyte. Reproduced with permission.[76] Copyright 2024, Royal Society of Chemistry.

which leads to two distinct electrolyte species in the system. Grignard compounds are known to be nucleophilic, which precludes the use of this electrolyte for electrophilic cathode materials such as sulfur and most organic materials as mentioned in the previous section. Apart from using Cl-containing additives, other types of halogens or halides have also been explored as additives for Mg electrolytes. For example, Li et al.[77] added a small concentration of iodine into the $Mg(TFSI)_2$/DME electrolyte, resulting in a reduced overpotential for Mg deposition/dissolution. Chinnadurai et al.[78] used $MgBr_2$ in $Mg(HMDS)_2$-based electrolyte, which also showed an improved reversibility.

An alternative strategy to limit the parasitic reactions between the Mg anode and electrolytes is to construct an artificial interphase that conducts Mg^{2+} ions. With the protection of a suitable interphase, it is expected that reversible Mg deposition can be enabled in conventional electrolytes. Son et al.[72a] reported an artificial Mg^{2+}-conducting interphase made from polyacrylonitrile (cPAN) and Mg triflate. This interphase can be engineered on the Mg anode surface, as shown in **Figure 7**. More importantly, the low electronic conductivity of this artificial interphase prevents the electrochemical reduction of the electrolyte, allowing the use of carbonate solvent, such as propylene carbonate (PC), even with moisture impurities. Compared to the pure Mg anode, the coated Mg anode demonstrated significantly enhanced reversible capacity and cycling stability in Mg/V_2O_5 full cells using $Mg(TFSI)_2$/PC electrolytes.

Except from using additives, an alternative approach involves anion modification. Huang et al. achieved this by modifying the OTf^- anion through grafting onto a fluorinated borate ester.[73] This approach yielded an asymmetric, weak-coordination boron-center anion ($[B(TFE)_3OTf]^-$, TFE = $-OCH_2CF_3$), using $CrCl_3$ as a catalyst to promote the process. Different quantities of $CrCl_3$ were tested to refine the synthetic pathway for the desired anion, and it was determined that 3wt% $CrCl_3$ is the optimal amount.

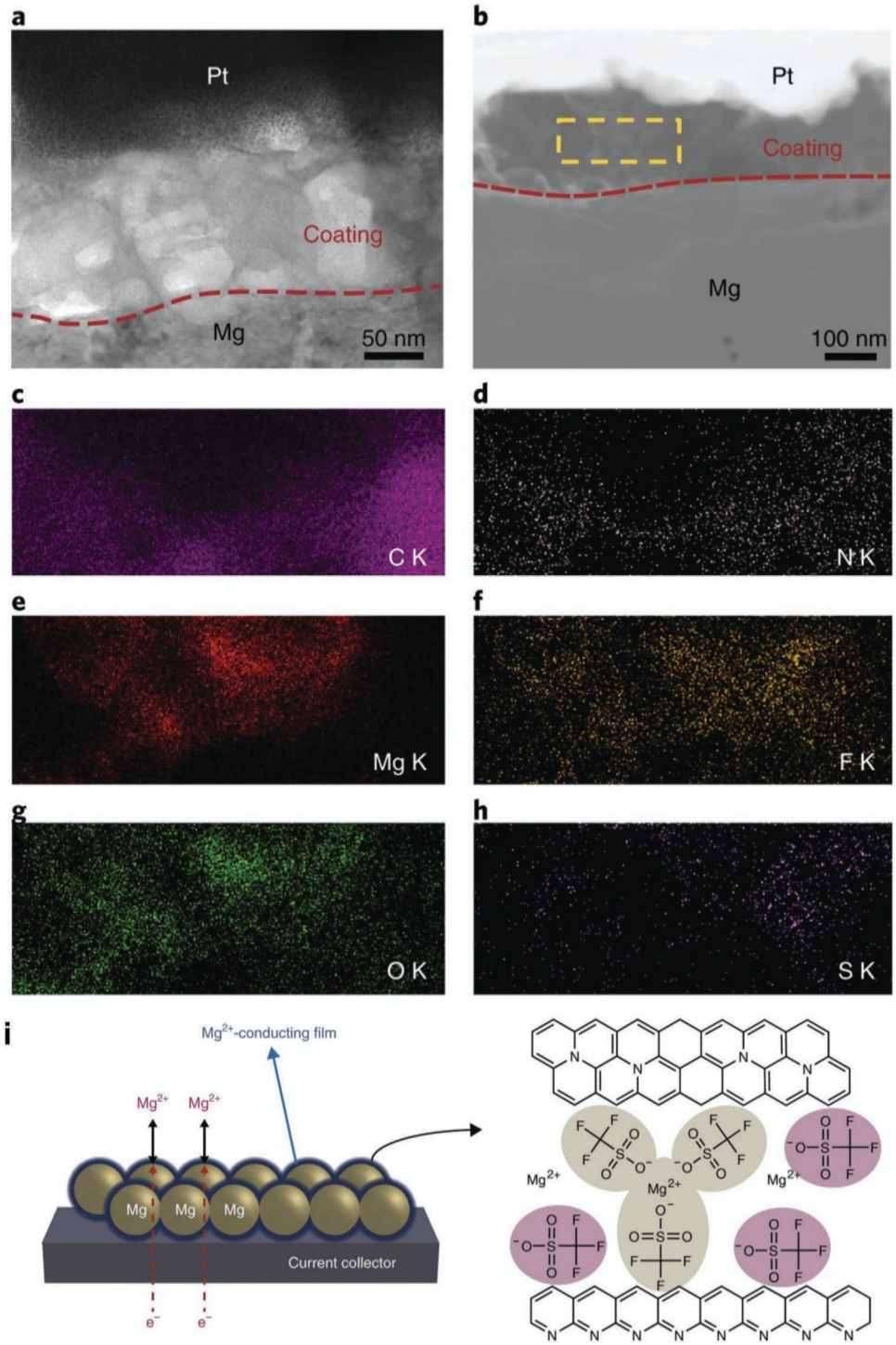

Figure 7. a) The coated Mg metal with the artificial Mg^{2+}-conducting interphase. Conformal coating thickness of 100 nm is observed on the Mg surface. b) STEM HAADF mode observation of Mg metal with the Mg^{2+}-conductive coating layer. STEM EDS mapping area is indicated by the yellow rectangular box. c–h) EDS mapping of c) C, d) N, e) Mg, f) F, g) O and h) S in the coating. i) Schematic of a Mg powder electrode coated with the artificial Mg^{2+}-conducting interphase, and the proposed structure for the artificial Mg^{2+}-conducting interphase based on XPS, TOF-SIMS, and TGA analysis. Reproduced with permission.[72a] Copyright 2018, Springer Nature.

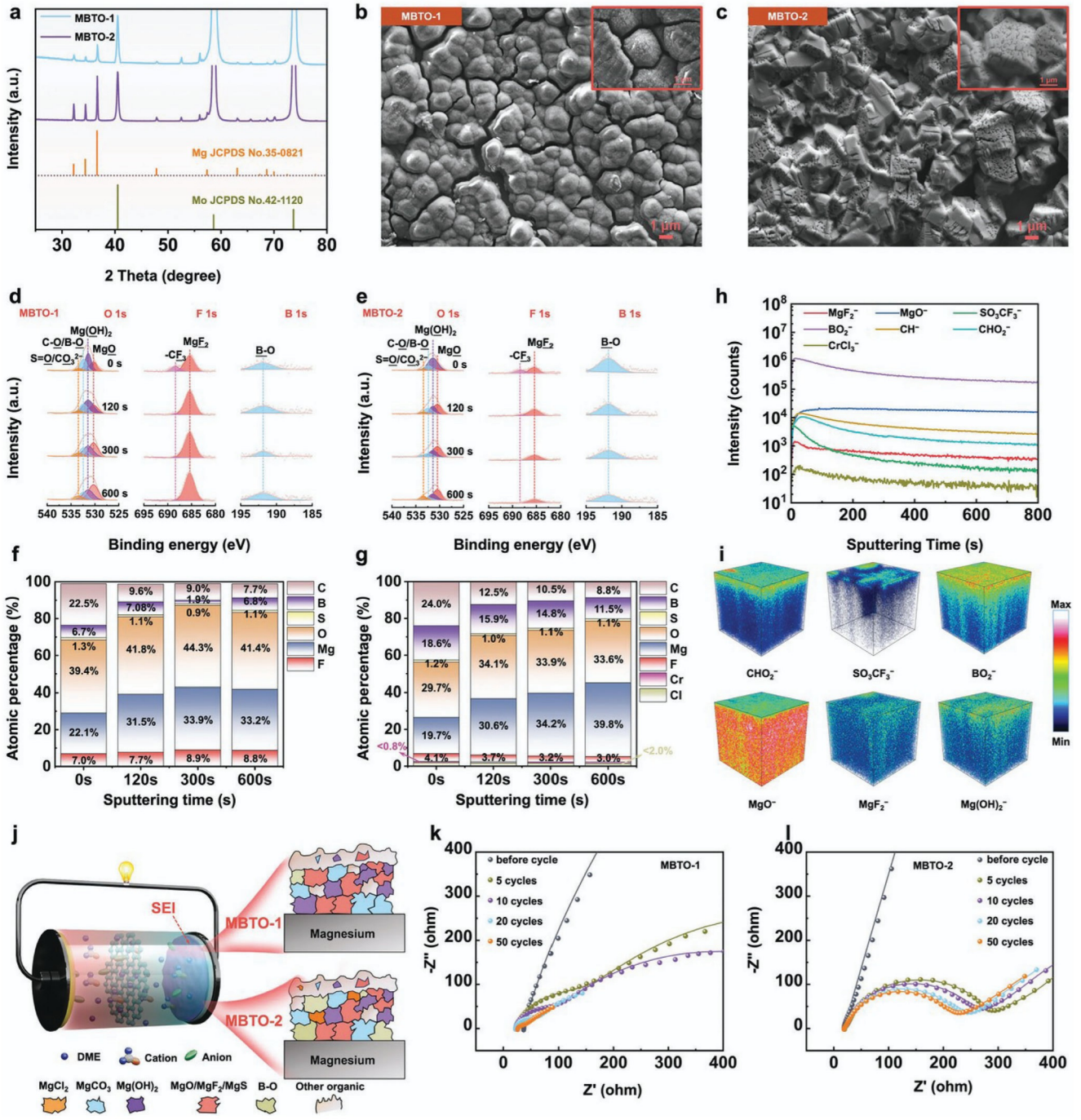

Figure 8. a) XRD patterns of the deposited Mg on Mo in MBTO-1 and MBTO-2 electrolytes. SEM images of the deposited Mg on Mo in b) MBTO-1 and c) MBTO-2 electrolytes. O 1s, F 1s, and B 1s XPS depth spectra of the deposited Mg on Mo after five cycles in d) MBTO-1 and e) MBTO-2 electrolytes. Elemental proportions of SEIs formed in f) MBTO-1 and g) MBTO-2 electrolytes. h) TOF-SIMS depth profiles and i) 3D rendering models of CHO_2^-, $SO_3CF_3^-$, BO_2^-, MgO^-, MgF_2^-, and $Mg(OH)_2^-$ for the deposited Mg on Mo after five cycles in MBTO-2 electrolyte. j) Schematic diagram of the SEI layer. EIS curves of Mg/Mg cells at the different cycles in (k) MBTO-1 and l) MBTO-2 electrolytes. Reproduced with permission.[73] Copyright 2024, John Wiley and Sons.

Both XPS and TOF-SIMS depth analysis confirm that only trace amounts of chloride (< 2 atomic%) were detected, indicating minimal introduction of soluble Cl^- ions into the electrolyte. **Figure 8** illustrates the morphology transition of the Mg deposits in electrolytes with different synthetic approaches, shifting from micron-sized spheres in the electrolyte synthesized without $CrCl_3$ (labeled as MBTO-1) to a crystalline hexagonal structure in the electrolyte synthesized with 3wt% $CrCl_3$ (labeled as MBTO-2). From the XPS and TOF-SIMS results, a B-containing organic/inorganic SEI film was formed on the surface. This film

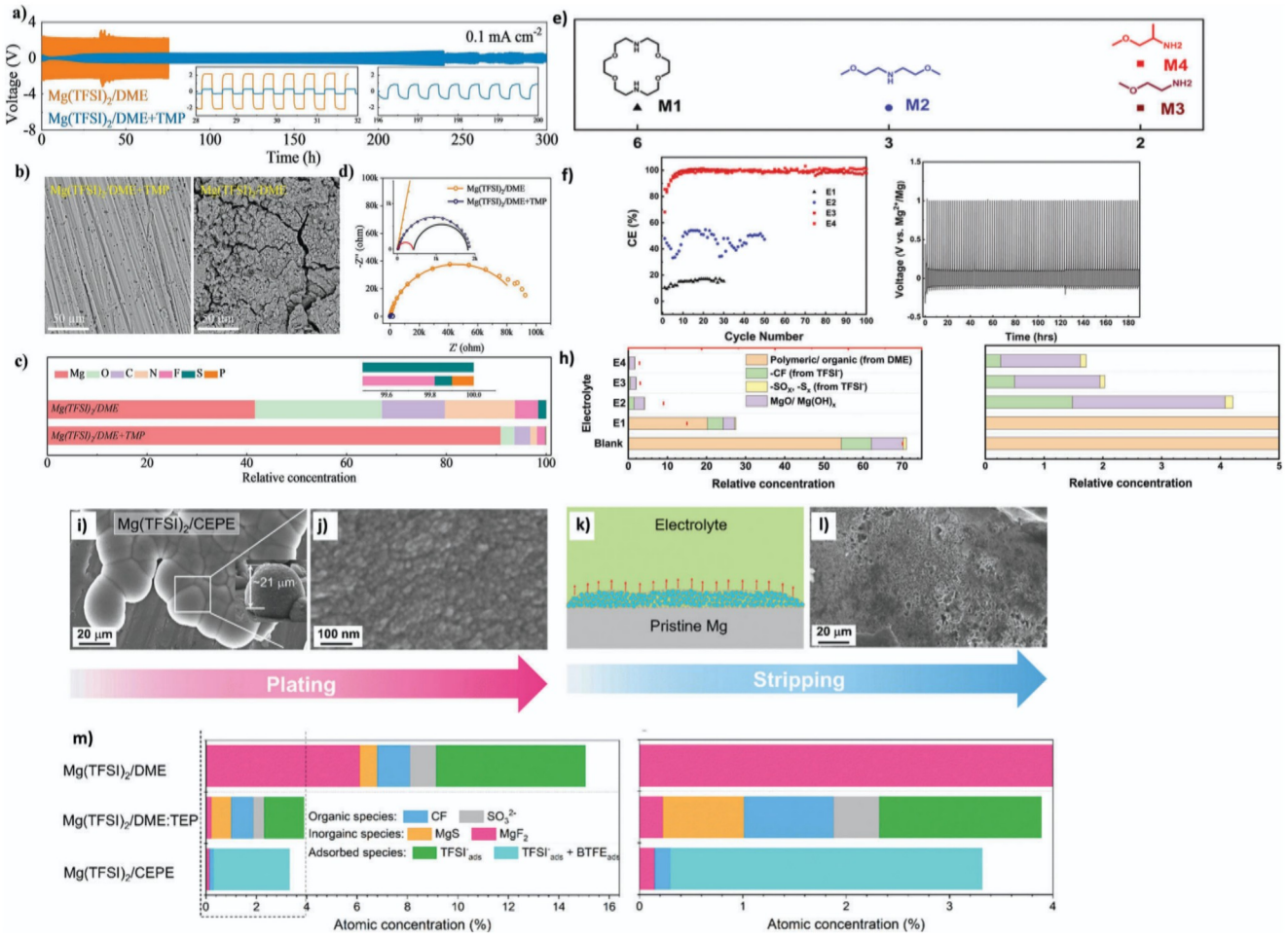

Figure 9. Electrochemical performance and morphological changes of Mg anode cycled in different electrolytes. a) Galvanostatic cycling of Mg||Mg symmetric cell with $Mg(TFSI)_2$/DME+TMP as the electrolytes at a current density of 0.1 mA cm^{-2}. The insets are the enlarged views of the curve at two specific time regions. b) SEM images of the 30th cycled Mg anode surface in the two electrolytes. c) Molar percentage of decomposition species found on the cycled Mg surface. The low content species information is shown in the inset. d) Nyquist plots of cells in the two different electrolytes. Reproduced with permission.[37] Copyright 2022, John Wiley and Sons. e) The molecular structure and denticity of the chelants. f) CEs for Mg plating and stripping in E_x in Mg||SS cells cycled at 0.1 mA cm^{-2}. g) Long-term cycling of the Mg||SS cell in E4 at a current density of 0.1 mA cm^{-2}. h) The relative concentrations of decomposition species found on the cycled Mg surface. Reproduced with permission.[3c] Copyright 2021, American Association for the Advancement of Science. i,j) Plated Mg morphologies in CEPE electrolyte. k) Schematic illustration of stripping current distribution on plated Mg. l) Fully stripped Mg morphologies in CEPE electrolyte. m) Atomic concentration of different $TFSI^-$-related species on the plated Mg surface and magnified view of the circled region. Reproduced with permission.[38] Copyright 2024, Royal Society of Chemistry.

played a dual role in enabling the reversible process of Mg plating/stripping while also demonstrating high compatibility with cathode materials, as reported. For selecting appropriate anions for Mg-ion conductive salts, the weakly ion-pairing approach appears to be the most promising direction, as it may facilitate the divalent ion transfer. Additionally, the anion decomposition on the metal anode surface should be taken into account, ideally forming beneficial SEIs, such as B-containing interphases.

Besides salt engineering, solvent coordination regulation is another effective approach that has been applied to address the interfacial issues between the anode and electrolyte. Zhao et al. applied trimethyl phosphate (TMP) as a solvent additive.[37] Due to the higher polarity of P═O double bonds, it can replace one of the three DME molecules in the solvation shell to form $[Mg(DME)_2TMP]^{2+}$. With the TMP electrolyte, the Mg||Mg symmetrical cells demonstrated a low overpotential, an extended cycle life and a low interfacial resistance as shown in **Figure 9**a,d. After 30 cycles of stripping/plating, the surfaces of Mg metal anodes taken from cells with different compositions were examined using SEM/EDX (Figure 9b,c). In different electrolytes, notable differences were observed in both the morphology and composition. In the electrolyte with TMP, the Mg surface appeared smoother with an Mg content over 90%. The remaining 10% comprises interphases resulting from the decomposition of the organophosphorus additive, which may facilitate the transport of Mg^{2+} as described in the work. Recently, a new co-ether phosphate electrolyte (CEPE) system combining a triethyl phosphate (TEP) additive with different ethers as co-solvents was reported to adjust the Mg^{2+} solvation sheath.[38] It was confirmed that the introduction of TEP successfully outcompeted the $TFSI^-$ anions

in the first solvation shell and enabled stable Mg^{2+}/Mg redox at the anode. The co-ether solvent played a crucial role in promoting a more uniform Mg deposition through nanoscale nucleation and growth, as shown in Figure 9i–l. A very thin SEI, characterized by trace amounts of S- and F-rich composition, was formed in this CEPE electrolyte (refer to Figure 9m). Interestingly, the absence of detectable TEP decomposition suggests no additive consumption within this system, which may also contribute to the long-term cycling stability.

Except from phosphate-based solvent/additives, a family of amine-based solvent/additive has also been studied by numerous researchers from various groups. For example, multidentate methoxyethyl-amine chelants [–($CH_2OCH_2CH_2N)_n$–] (M_x) with high affinity were chosen to reorganize the solvation sheath for Mg^{2+} ions (Figure 9e).[3c] The chelating agents facilitate the formation of a less compact and more polarizable solvation sheath. This favors electron transfer, thereby reducing overpotential and promoting stable Mg plating and stripping, as illustrated in Figure 9f,g. An additional intriguing observation from Figure 9h could shed light on the origins of the reduction in overpotentials. This reduction may correlate with the suppression of interfacial reactions or electrolyte decomposition, thus imposing a limitation on the thickness of the passivation layer. Using similar nucleophilic amidogen donor, Du et al.[40] introduced 2-methoxyethylamine (MOEA) into a simple $Mg(OTf)_2$/ether solution to compete in solvation coordination. Wang et al.[74b] proposed a series of solvent molecules with $Mg(TFSI)_2$ salt, including 3-methoxypropylamine and 1,3-propanediamine. It was proved that 3-methoxypropylamine, which has a moderate coordination ability, can be used as an effective solvent. Wang et al.[74a] added the 3-dimethylaminopropylamine (DMAPA) to the $Mg(TFSI)_2$/G2 electrolyte. The co-solvents can be partially ionized to form active ionic species, which help mitigate the decomposition of the $TFSI^-$ anion on the Mg metal anode. Recently, Li et al.[74c] selected a series of methoxy-amine-based electrolytes with different ion-pairing strength to explore their interfacial reduction stabilities and decomposition behaviors on a Mg metal anode. The conclusion is that the structures with strong cation-solvent coordination reduces the reduction stability against Mg anode, primarily due to hydrogen evolution from the amine group. To sum up, the solvation structure is closely related to the solubility of the electrolyte salt, electrochemical processes and interfacial parasitic reactions. When choosing a solvent or co-solvent, the solvation properties should be carefully considered. The ideal solvation structure would have low energy barriers in both the charge transfer and desolvation processes, while avoiding parasitic reactions, such as reduction on the Mg metal anode.

3.2.2. Organoborate-Based Electrolytes

Electrolytes based on magnesium organoborates emerge as promising candidates for the high-energy Mg batteries, given their elevated anodic stability, substantial ionic conductivity, and non-corrosive characteristics. In the system with fluorinated alkoxyborate-based electrolyte $Mg[B(hfip)_4]_2$/DME (hfip = $OC(H)(CF_3)_2$), the solvent coordinated $[Mg(DME)_3]^{2+}$ ion still stands out as the predominant species. The $[B(hfip)_4]^-$ anion decomposition was detected at the Mg anode, forming a MgF_2 and boron-based thin solid interphase.[79] MgF_2 has been demonstrated to possess ionic conductivity while lacking electronic conductivity, making it a favorable component for the SEI.[80] Thus a stable Mg stripping/plating behavior could be achieved with the $Mg[B(hfip)_4]_2$/DME electrolyte. Recently, a systematic study was conducted by Li et al.[81] to investigate the impact of anions in electrolytes using DME as the solvent. The anions ranging from 0 to 5 exhibit diverse -CF_3 substitutions shown in **Figure 10**a. The corresponding Mg^{2+} solvation shell can be divided into three categories with these anions (Figure 10b–d): close-contact solvation structure (anions 0 and 1), exhibiting a lower dissociation degree and an anion-derived passivation layer; completely dissociated solvation structure (anions 2 and 3), exhibiting a high dissociation degree with a high ionic conductivity and partially dissociated solvation structure (anions 4 and 5). From the experimental results, these solvates exhibit nearly identical decomposition products with similar decomposition degree, comprising both organic (C–O, B–O, C–F) and inorganic (Mg–F/Mg–O) components originating from the decomposition of various anions and the DME solvent. At the same time, the deposited Mg showed a polygonal structure (see Figure 10e,f). Beyond the lattice fringes of the bulk Mg, small amorphous layers were sparsely distributed, indicating that the interphases of this system do not densely cover the Mg surface. This observation contrasts with the behavior of Ca analogues, which will be discussed in detail in Section 3.3.3. It is hypothesized that the morphology of the interface will influence ion transport and, consequently, the electrochemical performance of the battery. Therefore, when aiming for an ideal SEI, its composition, thickness, and morphology should be considered simultaneously.

3.2.3. Carborane-Based Electrolytes

The unique properties of recently developed Mg carborane electrolytes, characterized by their nonreactivity toward moisture and noncorrosive nature, have been previously highlighted. By using scanning transmission electron microscopy (STEM) analysis, Singh et al. studied the interface of the Mg anode in $[Mg(DME)_3](CB_{11}H_{12})_2$ (MMC)/G4 electrolyte.[82] After galvanostatic cycling, the black deposits were characterized via TEM in cells with two different electrolytes: MMC electrolyte (**Figure 11**a–d) and all-phenyl-complex (APC) electrolyte (Figure 11e,f). In the APC electrolyte, the deposition appears as a compact crystalline structure without the presence of an SEI layer on the surface. Conversely, in MMC, an amorphous layer, comprising carbon and boron species as identified by XPS and TEM analysis, is observable outside the deposited Mg nanoparticles. The behavior of SEI formation corresponds to the Coulombic efficiency for Mg deposition and stripping. In the APC electrolyte, the Coulombic efficiency was 100%, indicating the absence of SEI presence. Conversely, in the MMC/G4 electrolyte, the Coulombic efficiency increased from 68 to 100% within the first four cycles, corresponding to SEI formation during the initial cycles. The increase in Coulombic efficiency with cycling is attributed to the formation of the interphase layer, facilitating efficient Mg metal growth and dissolution. Thus, the formation of this Mg-ion conductive SEI is crucial for the generation of active metal nanoparticles. This study confirms that interphase chemistry significantly

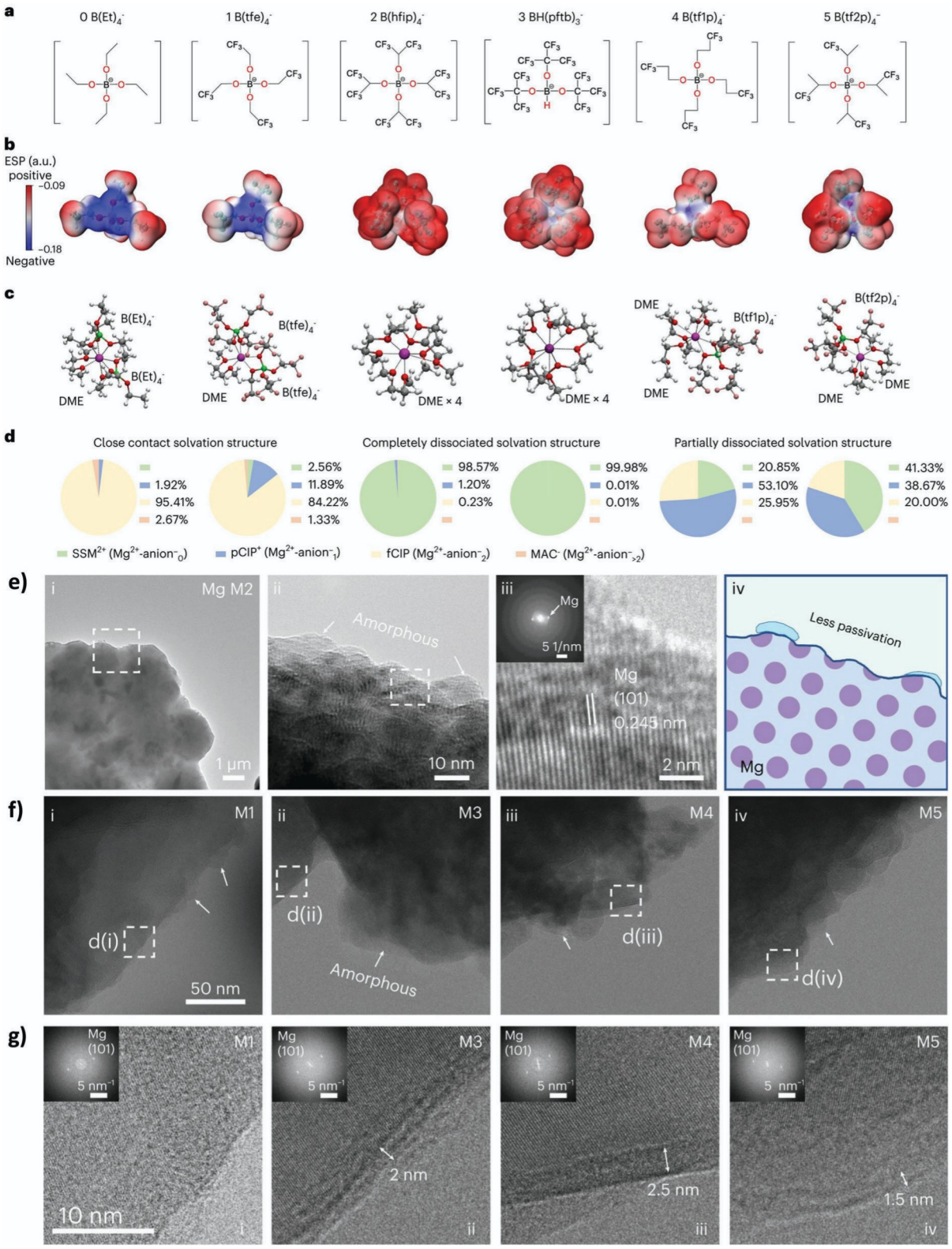

Figure 10. a) Molecular structure of six anions. b) Calculated ESP maps of anions under DME conditions. c) Typical solvation structure for the primary Mg^{2+} solvation shell obtained from MD simulations. Color scheme of molecules: Mg, purple; F, pink; O, red; C, gray; B, green; and H, white. d) Distribution of the Mg^{2+} solvates for the six electrolytes. e) Nanostructure of Mg deposited in the M2 electrolyte imaged by cryo-EM. f) Structure of deposited Mg in the M1/M3/M4/M5 electrolytes (arrows refer to amorphous passivation layers). g) Lattice fringes and FFT diffraction of deposited Mg. Reproduced with permission.[81] Copyright 2024, Springer Nature.

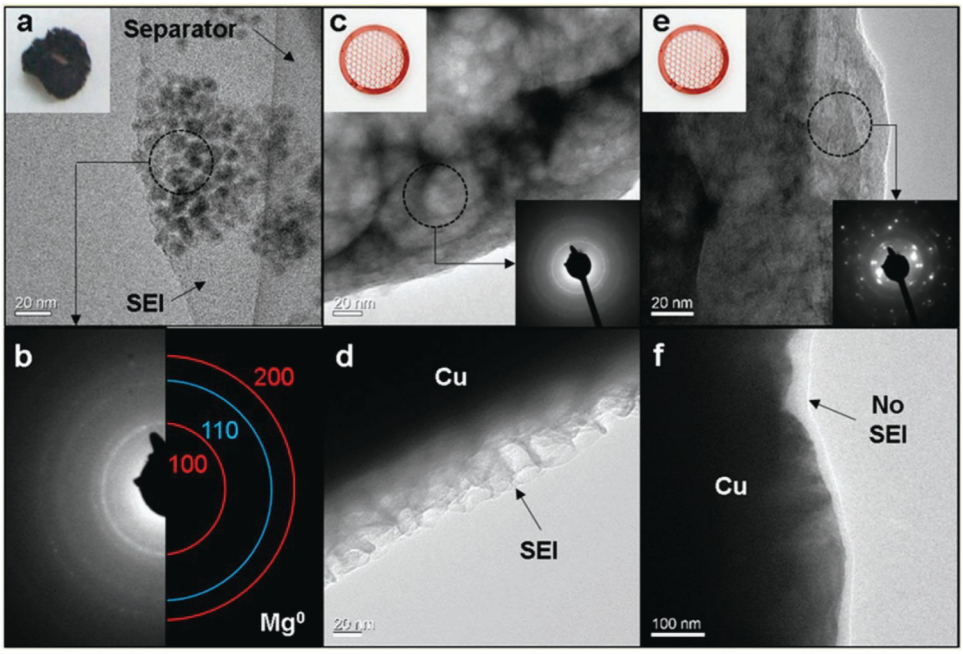

Figure 11. a) TEM image of a separator (inset) sample extracted from an Mg/Mg symmetrical cell after 100 cycles at 0.1 mA cm^{-2} (at 0.5 mA h) in MMC/G4. b) The corresponding SAED pattern for the material circled in (a). c) TEM image of a Cu grid sample extracted after 9.5 cycles (after deposition of Mg) at 0.1 mA cm^{-2} (at 0.5 mA h) in MMC/G4. d) TEM image of a Cu grid sample extracted after 10 cycles (after dissolution of Mg) at 0.1 mA cm^{-2} (at 0.5 mA h) in MMC/G4. e) Repetition of experiment c) except with APC electrolyte. f) Repetition of experiment d) except with APC electrolyte. Please note that the light contrast fringe in (f) is due to a slightly under focused TEM image and not an SEI layer. Reproduced with permission.[82] Copyright 2018, American Chemical Society.

influences the ability of Mg electrolytes to deposit and dissolve Mg metal. Apart from the variation in electrolyte composition, the separator also plays a crucial role, affecting the morphology of metallic deposits. However, addressing the influence of separator falls beyond the scope of this review paper.

3.3. Ca Interface Chemistries

The challenges associated with the interface between the Ca metal anode and the electrolyte are quite substantial, even more pronounced than those observed with Mg metal anodes. The presence of a passivating layer at this interface is quite critical, hindering ion transport and inhibiting metal deposition. Addressing these interfacial issues is essential to overcome this limitation. Thus, the establishment of a stable and electrochemically active interface between the Ca anode and electrolyte is important for improving the performance, safety, and cycle life of Ca metal batteries. This section aims to elucidate recent advancements in understanding Ca dissolution, deposition, and the resulting interfaces, focusing on the most promising electrolyte systems identified to date.

3.3.1. $Ca(BF_4)_2$

As previously discussed, $Ca(BF_4)_2$ exhibited a promising Ca metal stripping/plating behavior in a solvent mixture of ethylene carbonate (EC) and propylene carbonate (PC) with a low overpotential of 0.1 V at 100 °C.[46] Whereas there was negligible Ca deposition observed when using $Ca(ClO_4)_2$ and $Ca(TFSI)_2$ salt. However, the Coulombic efficiency was found to be quite low due to the difference in charge amount between Ca stripping and plating, suggesting the occurrence of undesired side reactions within the electrolyte during the Ca deposition process. Results from synchrotron X-ray diffraction experiments revealed a significant presence of CaF_2 in the deposits, likely a byproduct of electrolyte decomposition and presumably a component of the surface passivation layer. In 2019, the reversible Ca stripping/plating behavior of the $Ca(BF_4)_2$ electrolyte was further validated through SEM imaging, which depicted a thin Ca deposit layer on a copper substrate, as shown in **Figure 12**.[51] The electrochemical tests were conducted under room temperature, during which no detectable CaF_2 was observed. The authors explained that the formation of CaF_2 may not be as predominant at room temperature as it is in high-temperature conditions. A more comprehensive study was reported later in 2020, expanding on previous findings and offering deeper insights.[83] The anode-electrolyte interface was characterized by various surface analysis techniques, including transmission electron microscopy (TEM), as illustrated in **Figure 13**a–d. The presence of calcium borates (such as tricoordinated boron) and fluoride was confirmed, and a substantial amount of organic species were also proposed through an assumed polymerization mechanism depicted in Figure 13e. This layer functions as an SEI by allowing the percolation of Ca^{2+} ions while restricting further reduction of the electrolyte. When this layer was applied to a stainless steel working electrode by precycling the clean stainless steel electrode in $Ca(BF_4)_2$ electrolyte, and subsequently disassembling it for use as a working electrode

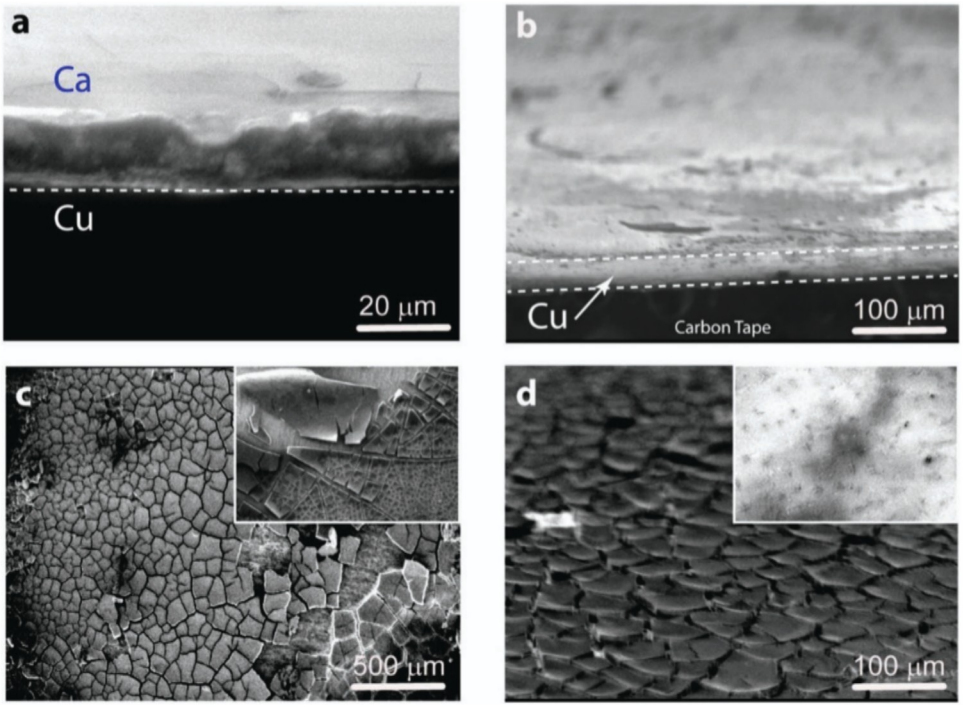

Figure 12. SEM images of the Cu substrate after different plating and stripping steps. a) Cross sectional image of the calcium deposit after the first plating. b) Image of the substrate after the first stripping. Dashed line in panel a visually aids to delineate the copper substrate from its surface, upon which calcium is deposited. The dashed lines in panel b delineate the cross sectional thickness of the Cu substrate, above which is the stripped surface and below which is carbon tape. c,d) Calcium deposits (appearing visually as thin grains) on the substrate as viewed from the top and from an angle, respectively, after the 10th plating (both images from the same sample). The inset of panel c shows the Cu substrate after the first plating, for comparison. The inset of panel d shows the Cu substrate surface after the 10th stripping. Reproduced with permission.[51] Copyright 2019, American Chemical Society.

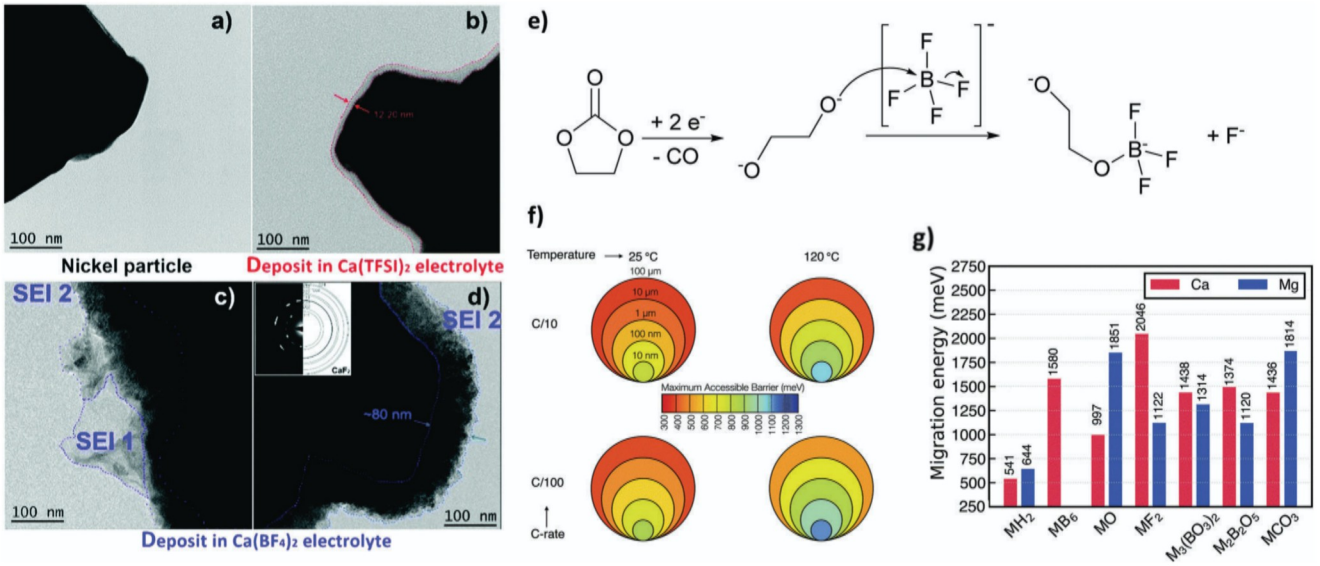

Figure 13. Bright field TEM images of Ni particles a) before and after formation of a surface layer in b) $Ca(TFSI)_2$ or c) and d) $Ca(BF_4)_2$ based electrolytes, respectively. Red and blue dotted lines are as a guide for the eye to indicate the thickness of each passivation layer. The inset in panel d) corresponds to the diffraction pattern associated to the deposit. e) Proposed mechanism for the anion decomposition upon reduction in $Ca(BF_4)_2$/EC:PC electrolytes. Further substitution of F by O can lead to cross-linked boron polymers. f) Maximum particle size tolerating reasonable diffusivity as function of M^{2+} migration energy in the context of battery performance at various charging rates and temperatures. g) energies of Ca^{2+} (red) and Mg^{2+} (blue) migration (*y*-axis in meV) in a number of materials as computed from first-principles calculations. M indicates either Ca^{2+} or Mg^{2+}. Reproduced with permission.[83] Copyright 2020, The Royal Society of Chemistry.

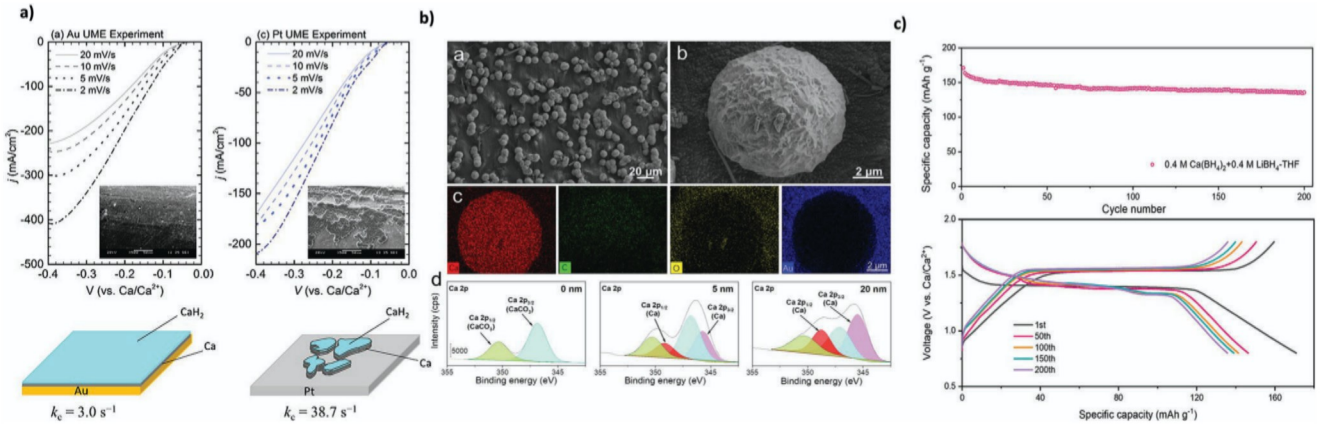

Figure 14. a) Experimental LSVs and schemes of proposed Ca electrodeposition in 1.0 M $Ca(BH_4)_2$ in THF at an Au UME and a Pt UME. Reproduced with permission.[84] Copyright 2019, American Chemical Society. b) Ca plating morphology in the $Ca(BH_4)_2$-$LiBH_4$-THF electrolyte at 0.25 mA cm^{-2} and 0.5 mAh cm^{-2}. And XPS depth profiling analysis of the deposits in the $Ca(BH_4)_2$-$LiBH_4$-THF electrolyte. The XPS sample was prepared by plating 0.5 mAh cm^{-2} of deposits on an Au electrode after 3 galvanostatic cycles at 0.25 mA cm^{-2} and 0.5 mAh cm^{-2}. c) The discharge specific capacity and voltage–capacity profile of LTO cathode material in a Ca||LTO full cell with the $Ca(BH_4)_2$-$LiBH_4$-THF electrolyte under galvanostatic cycling at 0.2C (1C = 175 mAh g^{-1}). Reproduced with permission.[85] Copyright 2020, John Wiley and Sons.

in another cell with a different electrolyte. Interestingly, it facilitated successful operation even in $Ca(TFSI)_2$/EC:PC electrolyte, a condition where pure stainless steel electrodes failed to achieve Ca deposition. This emphasizes the importance of borates as an essential element within the SEI layer. Building on the vital role of a borate-based layer in Ca plating, the same research group later explored boron trifluoride diethyl etherate as an additive in the $Ca(TFSI)_2$ electrolyte.[52]

Furthermore, the energy barriers for the migration of either Mg^{2+} or Ca^{2+} in selected materials were calculated and summarized in Figure 13f,g. These migration barriers vary with different conditions, such as temperature, thickness, and compositions. Although Mg/Ca compounds exhibit similarities in certain properties, the ion migration energy barriers show distinct trends. For example, Ca^{2+} has a much lower migration energy in oxides than in fluorides (997 meV vs 2046 meV), whereas the opposite trend is observed for Mg^{2+} (1851 meV for oxides vs 1122 meV for fluorides), as illustrated in Figure 13g. Notably, the migration energy barrier of Mg^{2+} in fluorides is significantly lower than that of Ca^{2+}. This implies that specific strategies are required in the design of optimal SEIs for the Mg/Ca battery systems, respectively.

3.3.2. $Ca(BH_4)_2$

As previously mentioned, Bruce et al. first reported the $Ca(BH_4)_2$ salt based electrolyte in THF solvent,[47] demonstrating the reversible plating and stripping of Ca with up to 94% Coulombic efficiency at room temperature. Borohydrides are recognized for their robust reducing properties and stability during electrochemical reduction processes. Analysis using X-ray diffraction (XRD) of the deposit formed with this electrolyte unveiled the presence of a minor amount of CaH_2 alongside the predominant Ca metal product. The formation of CaH_2 may be attributed to the reaction between Ca anode and THF ($Ca + C_4H_8O \rightarrow CaH_2 + C_4H_6O$), which may occur on Ca surface both during open circuit and Ca deposition to prevent continuous Ca reaction with electrolyte. However, authors mentioned that CaH_2 cannot effectively function as the SEI due to its limited ionic conductivity. Ultramicroelectrodes (UMEs) including Au and Pt were used by Ta et al. to further investigate Ca electrodeposition mechanism and speciation process with the same electrolyte.[84] There are three primary steps involves: 1) absorption of hydride ions on the electrode; 2) reduction of Ca^{2+} to metallic Ca on the electrode; 3) formation of CaH_2 on the metallic Ca. The experimental results have revealed that THF does not undergo decomposition upon exposure to Ca, indicating that the hydride does not originate from THF but rather from borohydride. Simulation results revealed that the first step occurring on the Pt electrode is ≈10 times faster than that on the Au electrode, which governs the diffusion time of adsorbed hydride, results in the formation of a patchy Ca layer on the Pt surface, whereas an even distribution is observed over the Au electrode, as depicted in **Figure 14a**. This observation hints at the dependency of metal electrodeposition on the substrates employed. Besides, Jie et al. emphasized that the solvation energy plays a pivotal role in influencing interfacial reactions on the electrode surface, ultimately determining electrochemical performance of the cells.[85] To decrease the coordination number of Ca^{2+} and weaken the solvation energy, $LiBH_4$ salt was introduced into the $Ca(BH_4)_2$/THF electrolyte. The addition of $LiBH_4$ was confirmed to induce the formation of a ball-shaped deposition composed of Ca, $CaCO_3$, CaO, and THF decomposition products, as illustrated in Figure 14b. Furthermore, when employing this electrolyte, the Ca||Au cells completed 200 discharge/charge cycles with a high Coulombic efficiency up to 99% and the calcium||lithium titanate (LTO) full cell exhibited stable performance over 200 cycles, as depicted in Figure 14c. In 2022, an in-depth investigation about the SEI in the model $Ca(BH_4)_2$/THF electrolyte was conducted with the help of TEM analysis under cryogenic conditions.[86] It's worth noting that in this work, a small amount of ≈0.004 M $NaBH_4$ was added to facilitate the formation of dense Ca deposits. It was demonstrated that instead of CaH_2, the interphase formed from the electrolyte

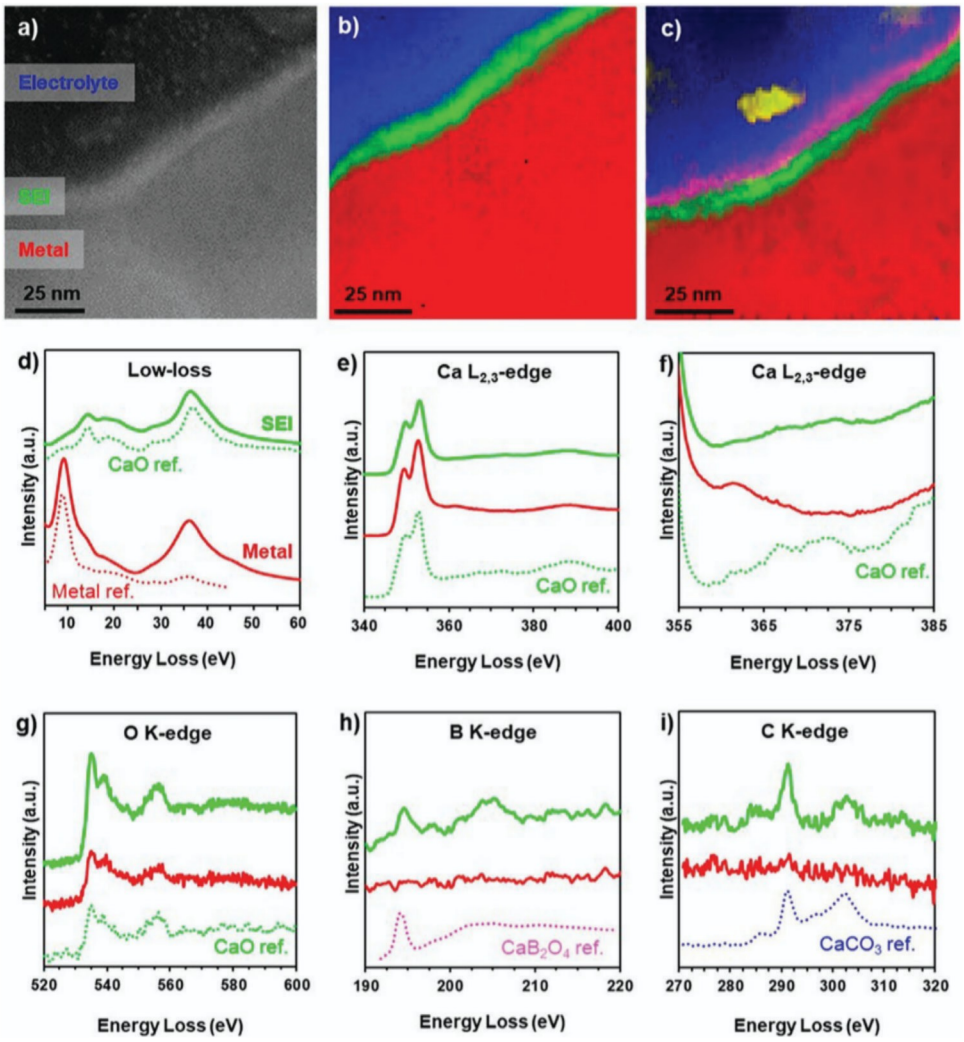

Figure 15. Compositional mapping of the interphase formed on the surface of a representative calcium deposit at cryogenic conditions. a) High-angle ADF-STEM image of calcium surface region highlighting interphase contrast. Corresponding b) LL and c) CL EELS maps in this approximate region at 1 nm/pixel resolution. d) Extracted LL-EELS spectra corresponding to the map in panel b. Extracted and background-subtracted CL-EELS spectra at the e) and f) Ca $L_{2,3}$-edge, g) O K-edge, h) B K-edge, and i) C K-edge corresponding to the map in panel c. At the B K-edge, a CaB_2O_4 referencespectrum is shown as an exemplar calcium borate species. Reproduced with permission.[86] Copyright 2022, American Chemical Society.

is a nanometric calcium oxide structure, with a small fraction of calcium borate and calcium carbonate species (**Figure 15**). The authors emphasized the significance of the nanoscale compositional and structural heterogeneity of the SEI in facilitating room-temperature Ca^{2+} transport through an otherwise ionically insulating material.

Recently, the coordination between Ca^{2+} and BH_4^- and solvation with THF has been investigated with various electrolyte concentrations via electrochemical quartz crystal microbalance with dissipation (EQCM-D).[87] The process of Ca deposition was unveiled to be more intricate than a straightforward two-electron mechanism. It encompasses the desolvation of THF and various configurational rearrangements within surface complexes, such as $CaBH_4^+ \cdot 4THF$ or $Ca(BH_4)_3^- \cdot 4THF$, as illustrated in **Figure 16**a. Figure 16b provides a summary of potential reaction pathways for Ca deposition in the $Ca(BH_4)_2$/THF system. The components of the interface layer were identified through XPS, as depicted in Figure 16c–e. These components include calcium oxide, borates, carbonate and some organic species, which align with previous reports.

Based on the discussed studies, it can be concluded that the interphases demonstrate variability, which is influenced by factors such as salt concentration, additives, substrates, and test conditions.

3.3.3. $Ca[B(hfip)_4]_2$ and $Ca[Al(hfip)_4]_2$

In 2019, a pioneering Ca electrolyte incorporating $Ca[B(hfip)_4]_2$ salt with DME solvent was reported by two separate research groups,[49] drawing inspiration from its Mg electrolyte counterparts as mentioned earlier in Section 3.2.2. The weakly coordinating organoborate anion leads to the formation of fully isolated solvates, in which the Ca^{2+} ion is coordinated by

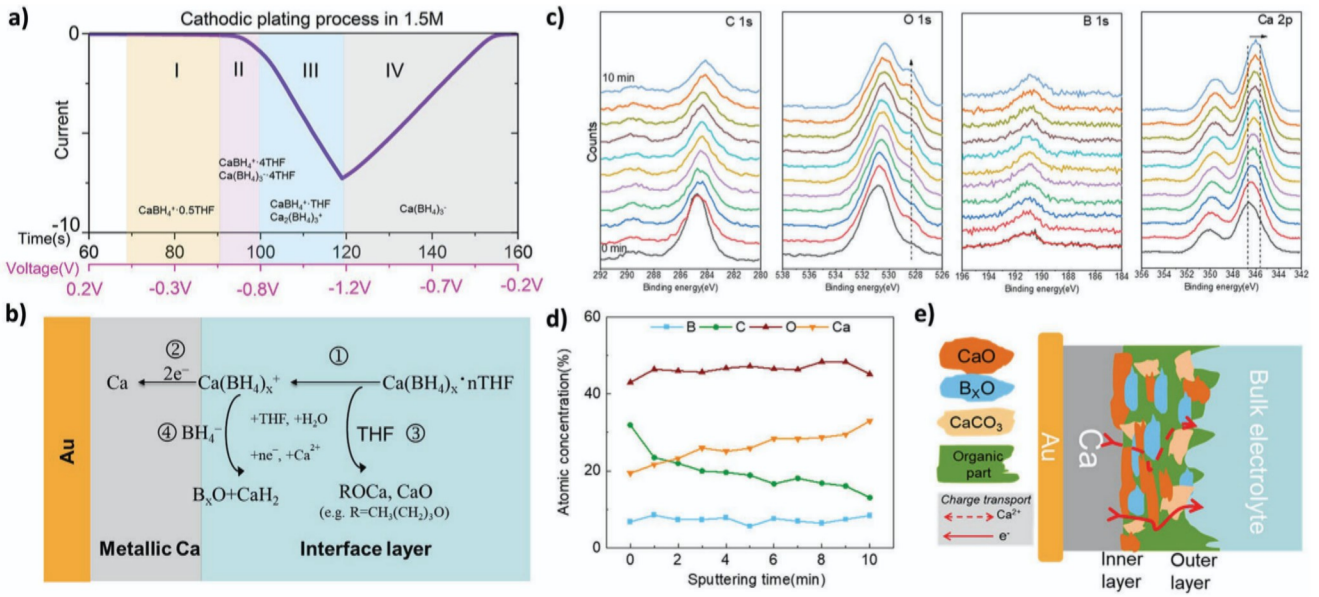

Figure 16. a) Proposed key surface intermediates identified by EQCM-D data on the Au surface in the 1.5 M electrolyte cell during the first cathodic plating process as a function of time (corresponding potential scale is shown in magenta, and b) scheme of the proposed surface electrochemical reaction pathways during the first Ca electrodeposition process for 1.5 M electrolyte. c) High-resolution XPS spectra of C 1s, O 1s, B 1s, and Ca 2p at select sputter depths on the plated Ca film in 1.5 M $Ca(BH_4)_2$/THF solution. d) Atomic concentrations of possible decomposition species throughout the depth profiling. e) Schematic illustration of the SEI layer formed on the plated Ca electrode in 1.5 M $Ca(BH_4)_2$/THF electrolyte. Reproduced with permission.[87] Copyright 2023, American Chemical Society.

four DME molecules, exhibiting a slightly distorted square antiprismatic coordination geometry. Li et al. demonstrated that 0.25 M $Ca[B(hfip)_4]_2$ in DME could achieve an ≈80% Coulombic efficiency.[49a] This was observed after a few conditioning cycles with an overpotential of ≈300 mV and an anodic stability above 4.5 V versus Ca. Shyamsunder et al. utilized the same salt at a slightly higher concentration, ≈0.5 M in DME, as an electrolyte.[49b] From their study, the Coulombic efficiencies of the cells in this electrolyte were above 90% after the fourth cycle but with a higher overpotential for the Ca deposition process, ≈550 mV. Besides, with the addition of a chloride salt (tetrabutylammonium chloride) as an additive in the electrolyte, previously employed in $Ca(BH_4)_2$/THF electrolyte,[84] the cycling life of the cell extended substantially. Moreover, it resulted in a further enhanced Coulombic efficiency, reaching up to 95%. The main deposits observed on the electrode were Ca metal and also some CaF_2, with no detection of CaH_2. The formation of fluoride deposits was attributed to the decomposition of the anions on the reductive Ca metal. With a high migration energy barrier of ≈2046 meV as shown in Figure 13g,[83] CaF_2 may impede the Ca^{2+} ion transport and passivate Ca surface, thereby limiting cycling stability of the anode. With the advancement of new technologies, recently, the nanoscopic structures of the deposit in the electrolyte with $Ca[B(hfip)_4]_2$/DME electrolyte were detected using cryo-electron microscopy (cryo-EM), as illustrated in **Figure 17**.[81] The deposition predominantly exhibited a spherical morphology, accompanied by an amorphous layer where many $CaCO_3$ and CaF_2 nanocrystals were identified. The layer continued growing on the Ca deposits, which could have a significant impact on ion transport. This study offered direct evidence of the morphology and composition of the interphases in the cells employing $Ca[B(hfip)_4]_2$/DME electrolyte. Later, other different solvents like THF and diglyme (DGM) were also evaluated for comparison with the DME solvent-based electrolyte.[55] Notably, the $Ca[B(hfip)_4]_2$/DGM electrolyte exhibited the lowest polarization and demonstrated the longest cycling stability in

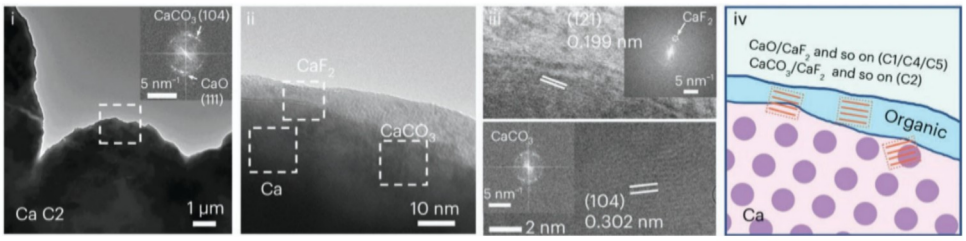

Figure 17. Nanostructure of deposited Ca and the passivation layer in the $Ca[B(hfip)_4]_2$/DME electrolyte. Reproduced with permission.[81] Copyright 2024, Springer Nature.

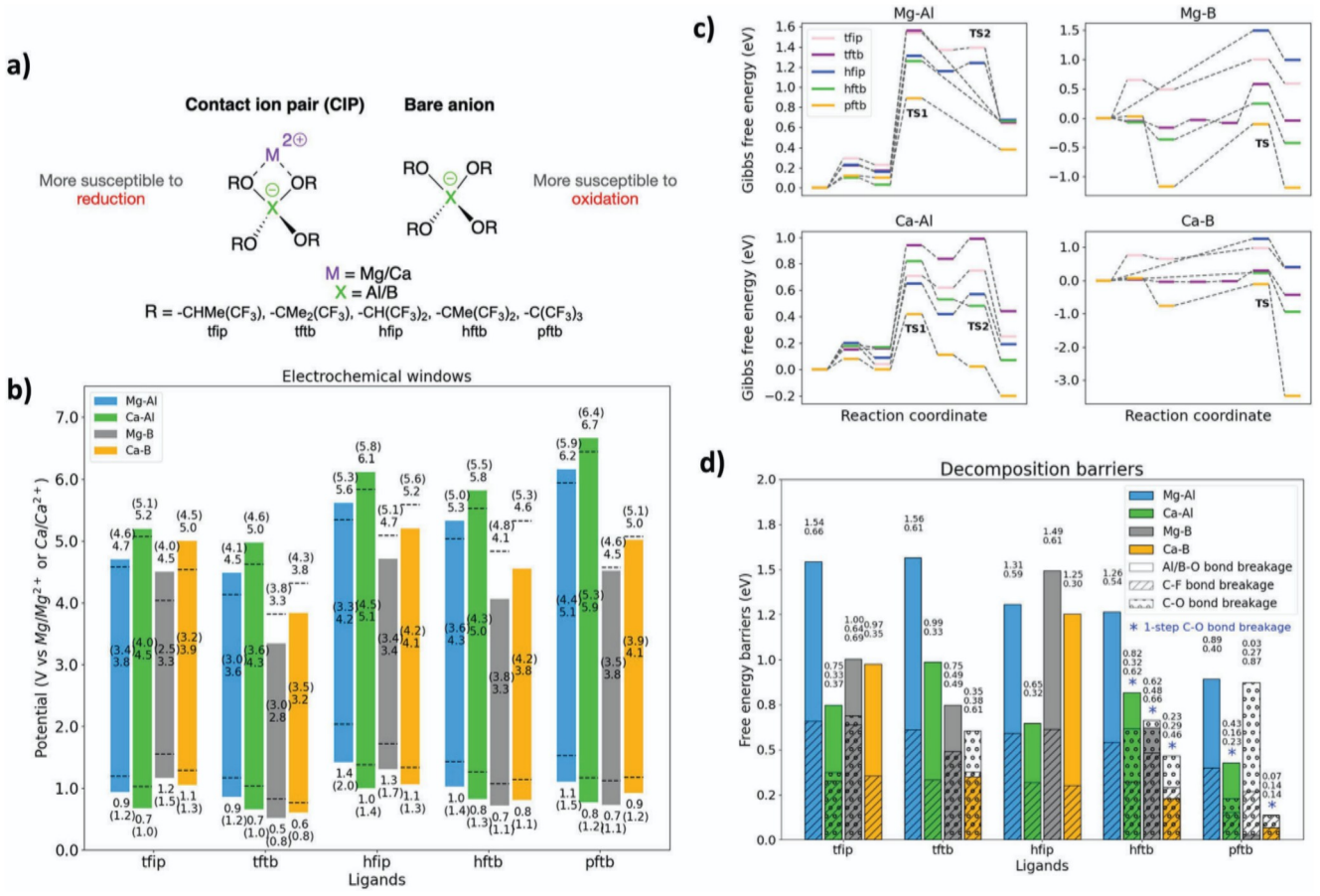

Figure 18. a) Concept of contact ion pairs (CIP) and bare anions. b) Electrochemical windows for the anions. Bare anions (X^- = monoanionic ligands) were used for oxidation potentials (upper limit) and contact ion pairs ($[M^{2+}X^-]^+$, M = Mg/Ca) were used for reduction potentials (bottom limit). Two levels of theory were used for comparison: the redox potentials shown in the regular bars are based on the ωB97X-D3/def2-TZVPPD/CPCM/RIJCOSX//ωB97X-D3/def2-SVPD/CPCM/RIJCOSX level of theory, whereas the black dashed lines and the numbers in parentheses are from the B3LYPD3BJ/def2-TZVPPD/CPCM//B3LYPD3BJ/def2-SVP/CPCM level of theory. The numbers in the middle of the bars are the energy gaps between the two redox potentials (stability windows). Decomposition pathways and rate-limiting barrier heights. c) Decomposition pathways for Al—O/B—O bond breakage. d) Rate-limiting decomposition free energy barriers for Al—O/B—O, C—F, and C—O bond breakage. The numbers on each bar from the top to bottom are the rate-limiting barriers for Al/B—O bond breakage, C—F bond breakage, and C—O bond breakage. Note that the C—O bond-breaking barrier is only shown when it is less than 1.0 eV. Reproduced with permission.[88a] Copyright 2022, American Chemical Society.

symmetric cells. Additionally, this cell displayed a dendrite-free morphology with predominantly smooth Ca deposits. This outcome might be attributed to variations in solvent coordination stability.

Due to the chemical similarity between B and Al, researchers have also explored alkoxyaluminate-based electrolytes for Ca batteries through both computational and experimental studies.[88] Based on the reduction of metal-coordinating anions and oxidation of bare anions, the theoretical electrochemical windows in different anion systems were calculated as shown in **Figure 18**a,b. The decomposition pathways for Al—O/B—O bond breakage and the corresponding decomposition energy barriers are depicted in Figure 18c,d. The results indicate that the fluctuations in decomposition barriers for borate salts are primarily influenced by steric factors, whereas electronic effects play a more crucial role in aluminate salts. And the tftb (-$CH(CH_3)_2CF_3$) ligand is identified as the most promising ligand for aluminate salts, as it exhibits the highest barrier for decomposition under reductive conditions, whereas the hfip ligand shows the most promise in the borate salt series. This suggests the necessity of considering distinct design rules for the future development of anion design for the electrolyte salts. Recently, an experimental work on the calcium tetrakis(hexafluoroisopropyloxy) aluminate salt, $Ca[Al(hfip)_4]_2$, was reported, further confirming the feasibility of this salt.[88b] Comparable electrochemical performances were reported using this aluminate salt in comparison with the borate salt, despite the more intricate synthesis process involved in the aluminate salt. Another noteworthy observation is the relatively low amounts of F and Al detected at the surface of deposits, as shown in **Figure 19**, indicating the relatively good stability of the aluminate salt anion. Therefore, in this system, the decomposition of coordinated solvent molecules from the cation solvation shell is recognized as the primary factor contributing to side reactions at the Ca metal/electrolyte interface.

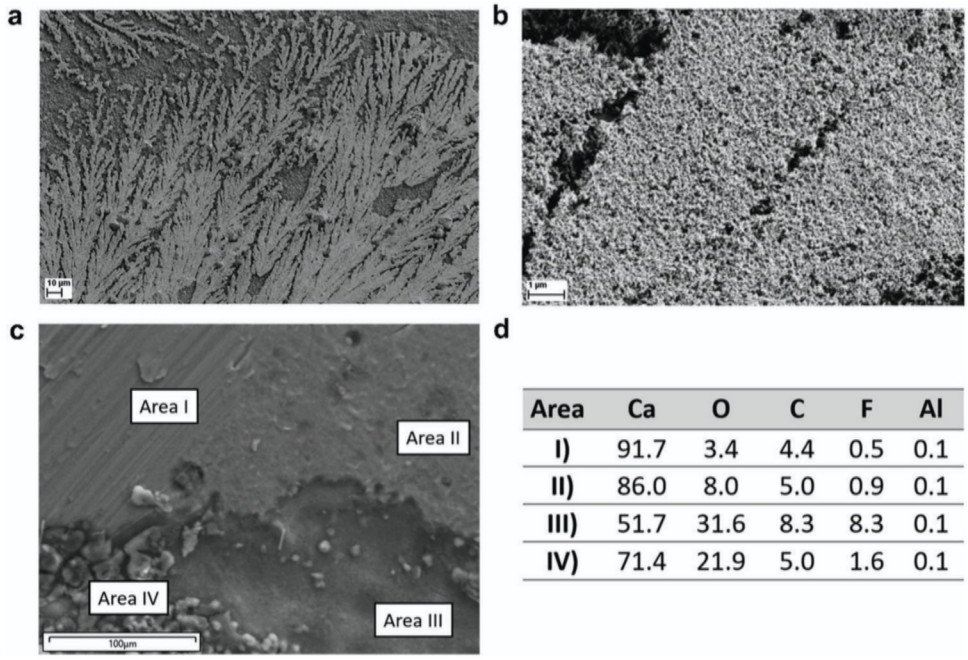

Area	Ca	O	C	F	Al
I)	91.7	3.4	4.4	0.5	0.1
II)	86.0	8.0	5.0	0.9	0.1
III)	51.7	31.6	8.3	8.3	0.1
IV)	71.4	21.9	5.0	1.6	0.1

Figure 19. a,b) SEM image of Ca deposits from the CaAlhfip/DME electrolyte on the carbon-coated Al foil at different magnifications revealing a dendrite-like morphology. c) SEM image of the Ca metal electrode from the Ca||Ca symmetric cell in the CaAlhfip/DME electrolyte with marked areas with different morphologies (I–IV). d) Corresponding EDX measurements. Reproduced with permission.[88b] Copyright 2023, Royal Society of Chemistry.

3.3.4. $Ca[CB_{11}H_{12}]_2$

As discussed in the previous sections, fluorine-containing electrolytes intrinsically induce CaF_2 formation on the electrode. With a high migration barrier, CaF_2 hinders Ca diffusion as well as the plating and stripping processes. Thus, realizing a fluorine-free system is desirable for practical Ca electrolytes. In 2021, a fluorine-free Ca electrolyte, utilizing calcium monocarborane ($Ca[CB_{11}H_{12}]_2$) in a binary mixture of THF and DME, has been proposed.[58] Featuring a weakly coordinating hydrogen cluster, this electrolyte demonstrated a wide electrochemical potential window of up to 4 V versus Ca^{2+}/Ca and a high ionic conductivity at 4 mS cm^{-1}. Additionally, it enabled reversible Ca metal plating and stripping at room temperature, achieving a promising Coulombic efficiency of ≈88%. The composition of the deposits on the Au electrode was characterized by XRD, revealing the prevalence of Ca metal in the form of α-Ca and β-Ca, along with a small amount of CaH_2. Spherical particles mainly composed of Ca, O, and C were observed on Au by SEM as shown in **Figure 20**. Besides, small amounts of B were also detected, likely originating from electrolyte reduction at low potentials or residual electrolyte. This electrolyte has been reported to be compatible with various cathode materials, such as sulfur and copper sulfide.[10e] Built upon this single salt electrolyte, a cosalt system incorporating both $Ca(BH_4)_2$ and $Ca[CB_{11}H_{12}]_2$ was also investigated. It was proved that $Ca(CB_{11}H_{12})^+$ serves as an effective Ca delivery species, attributed to its low desolvation barrier and structural flexibility. And the reduction of Ca from $Ca(CB_{11}H_{12})^+$ is both kinetically and thermodynamically more favorable compared to $CaBH_4^+$.[59]

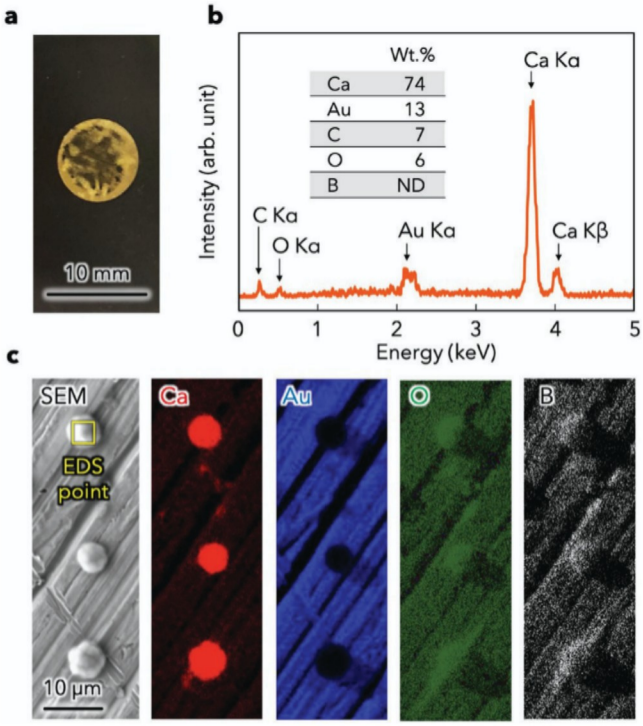

Figure 20. a) Optical image of the Au electrode after a Ca plating process. b) Energy-dispersive X-ray spectroscopy (EDS) profile within the yellow square. c) Scanning electron microscopy (SEM) image of Ca deposits on the Au electrode after Ca plating in an Au|$Ca[CB_{11}H_{12}]_2$/DME/THF|Ca cell, and EDS maps of Ca, Au, O, and B. Reproduced with permission.[58] Copyright 2021, Springer Nature.

4. Summary and Perspectives

Post-lithium battery systems are currently gathering attention, driven by the continuous debate surrounding the sustainability of lithium-based battery technology and the potential risks associated with the future availability of certain raw materials, like lithium, cobalt and nickel. Although the advancement of divalent metal batteries is underway, they are still in the nascent stages of development, indicating that a considerable journey lies ahead before their practical benefits can be fully realized. This review provides a comprehensive summary of the existing electrolytes utilized in divalent metal batteries, revisits the formation mechanism of the anode-electrolyte interface, identifies relevant components, and highlights recent advancements in addressing interfacial challenges associated with divalent metal anodes. Based on the development of the divalent metal batteries and the encountered interfacial issues, we outline the following perspectives:

1) The anode interfacial properties are determined by the chemical or electrochemical interactions of the metal anodes with the electrolyte component species, including solvents, anions additives and impurities. Therefore, the analysis of the formulation and understanding the ion-pairing as well as the solvation properties of the electrolytes are the fundamental requirements in addressing the challenges related to the anode-electrolyte interface in divalent metal batteries. By taking advantage of facile dissociation processes at the interfaces, weakly ion pairing approach by anion design paves the way for the development of efficient electrolytes. When selecting solvents, their solvation ability plays vital role for the electrochemical and interfacial properties of the electrolytes and anodes, respectively. The ideal solvation structure should feature low energy barriers during both charge transfer and desolvation processes, while avoiding parasitic reactions such as reduction on the metal anode. Furthermore, it should be noted that while Mg/Ca systems share some similarities, the optimal electrolyte components for Mg/Ca battery systems should be independently considered due to their unique intrinsic ion properties, such as charge density, solvation structures, and coordination chemistries. Moving forward, the development of solid or quasi-solid electrolytes holds promise for minimizing the organic solvent usage, which could be beneficial for addressing issues related to the anode interface and battery safety. Moreover, greater emphasis should be placed on identifying appropriate solid-state conductors with high ionic conductivity for divalent Mg^{2+} and Ca^{2+}. Besides, this approach also imposes more stringent requirements on the advancement of cathode materials.
2) Due to the strong reducing nature of divalent metals, it is essential to minimize the presence of traces of oxygen, water, and other organic vapors in the glovebox. These impurities can react with the metal anode, resulting in the formation of oxides and hydroxides on the surface. While these species may be electrochemically stable, they are inert and can hinder the intrinsic electrochemical performance of the metal anode. Therefore, attention should be paid not only to choosing the proper electrolyte salt and solvent but also to the purification degree of electrolytes and the cleanliness of the glovebox atmosphere during battery preparation and assembly.
3) Developing interfacial science and optimizing the anode/electrolyte interface are of paramount significance for building safe and efficient divalent metal batteries. The persistent understanding of the cation solvation and the underlying chemical/electrochemical processes through collaborative experimental and theoretical research is required. Several specific approaches have been explored to optimize the interface. One promising method involves direct and straightforward modification of the divalent metal surface using designed artificial coating materials before battery assembly. However, challenges arise in maintaining the integrity of the artificial layer during metal stripping/plating processes. A more promising and simple approach is utilizing functional electrolyte additives to optimize the system and establish an interphase during rest or cycling. By forming ionically conductive interphases on the metal electrode, this approach can help prevent surface passivation during the dynamic electrochemical process, thereby preserving the electrochemical activity of metal anode and ensuring the reversibility of the battery.
4) It can be summarized that the physical, chemical, and electrochemical properties of the interface critically influence ion transport, metal nucleation/growth, and thereby impact the electrochemical performance of the cell. A wide range of spectroscopic and diffraction techniques, both in situ and ex situ, can be utilized to uncover the morphological/compositional evolution of interphases, offering complementary perspectives on the dynamic processes occurring at the electrode-electrolyte interface. By leveraging these diverse characterization approaches, researchers can gain a comprehensive understanding of the interfacial phenomena and the correlations between interface formation and electrochemical properties of batteries. This knowledge facilitates the rational design of electrolytes and interfaces tailored to promote fast ion transport and enhance battery stability.

Acknowledgements

This work was funded by the Federal Ministry of Education and Research (Bundesministerium für Bildung und Forschung, BMBF) of Germany within the project "CaSino" (03XP0487F) and the German Research Foundation (DFG) under Project ID 390874152 (POLiS Cluster of Excellence). This work contributes to the research performed at CELEST (Center for Electrochemical Energy Storage Ulm-Karlsruhe). [Correction added on August 2, 2024, after first online publication: Acknowledgement Section has been corrected.]

Open access funding enabled and organized by Projekt DEAL.

Conflict of Interest

The authors declare no conflict of interest.

Keywords

anode-electrolyte interface, calcium metal battery, electrolyte, magnesium metal battery, metal anode

Received: May 17, 2024
Revised: July 15, 2024
Published online: July 31, 2024

[1] a) J. B. Goodenough, Y. Kim, *Chem. Mater.* **2010**, *22*, 587; b) F. Degen, M. Winter, D. Bendig, J. Tübke, *Nat. Energy* **2023**, *8*, 1284; c) F. Wu, J. Maier, Y. Yu, *Chem. Soc. Rev.* **2020**, *49*, 1569; d) A. Manthiram, *ACS Cent. Sci.* **2017**, *3*, 1063.

[2] a) J. W. Choi, D. Aurbach, *Nat. Rev. Mater.* **2016**, *1*, 16013; b) J. Muldoon, C. B. Bucur, T. Gregory, *Chem. Rev.* **2014**, *114*, 11683; c) Y. Liang, H. Dong, D. Aurbach, Y. Yao, *Nat. Energy* **2020**, *5*, 646.

[3] a) D. Monti, A. Ponrouch, R. B. Araujo, F. Barde, P. Johansson, M. R. Palacín, *Front. Chem.* **2019**, *7*, 00079; b) H. D. Yoo, I. Shterenberg, Y. Gofer, G. Gershinsky, N. Pour, D. Aurbach, *Energy Environ. Sci.* **2013**, *6*, 2265; c) S. Hou, X. Ji, K. Gaskell, P.-f. Wang, L. Wang, J. Xu, R. Sun, O. Borodin, C. Wang, *Science* **2021**, *374*, 172.

[4] a) R. J. Gummow, G. Vamvounis, M. B. Kannan, Y. He, *Adv. Mater.* **2018**, *30*, 1801702; b) M. E. Arroyo-de Dompablo, A. Ponrouch, P. Johansson, M. R. Palacín, *Chem. Rev.* **2020**, *120*, 6331.

[5] D. Aurbach, Z. Lu, A. Schechter, Y. Gofer, H. Gizbar, R. Turgeman, Y. Cohen, M. Moshkovich, E. Levi, *Nature* **2000**, *407*, 724.

[6] M. Hayashi, H. Arai, H. Ohtsuka, Y. Sakurai, *J. Power Sources* **2003**, *119–121*, 617.

[7] J. D. Forero-Saboya, D. S. Tchitchekova, P. Johansson, M. R. Palacín, A. Ponrouch, *Adv. Mater. Interfaces* **2022**, *9*, 2101578.

[8] a) E. M. Erickson, E. Markevich, G. Salitra, D. Sharon, D. Hirshberg, E. de la Llave, I. Shterenberg, A. Rosenman, A. Frimer, D. Aurbach, *J. Electrochem. Soc.* **2015**, *162*, A2424; b) D. Li, Y. Yuan, J. Liu, M. Fichtner, F. Pan, *J. Magnesium Alloys* **2020**, *8*, 963; c) D. Aurbach, H. Gizbar, A. Schechter, O. Chusid, H. E. Gottlieb, Y. Gofer, I. Goldberg, *J. Electrochem. Soc.* **2001**, *149*, A115; d) Z. Lu, A. Schechter, M. Moshkovich, D. Aurbach, *J. Electroanal. Chem.* **1999**, *466*, 203; e) G. Bieker, V. Küpers, M. Kolek, M. Winter, *Commun. Mater.* **2021**, *2*, 37.

[9] K. Jayasyaee, R. Rerthelot, K. C. Lethesh, E. M. Sheridan, *Magnesium Batteries: Research and Applications*, Royal Society of Chemistry, London **2019**, pp. 114–141.

[10] a) Q. Wei, L. Zhang, X. Sun, T. L. Liu, *Chem. Sci.* **2022**, *13*, 5797; b) Z. Meng, A. Reupert, Y. Tang, Z. Li, G. Karkera, L. Wang, A. Roy, T. Diemant, M. Fichtner, Z. Zhao-Karger, *ACS Appl. Mater. Interfaces* **2022**, *14*, 54616; c) Z. Li, B. P. Vinayan, T. Diemant, R. J. Behm, M. Fichtner, Z. Zhao-Karger, *Small* **2020**, *16*, 2001806; d) X. Yu, M. J. Boyer, G. S. Hwang, A. Manthiram, *Adv. Energy Mater.* **2019**, *9*, 1803794; e) K. Kisu, R. Mohtadi, S.-I. Orimo, *Adv. Sci.* **2023**, *10*, 2301178.

[11] H. Wang, J. Ryu, Y. Shao, V. Murugesan, K. Persson, K. Zavadil, K. T. Mueller, J. Liu, *ChemElectroChem* **2021**, *8*, 3013.

[12] L. W. Gaddum, H. E. French, *J. Am. Chem. Soc.* **1927**, *49*, 1295.

[13] T. D. Gregory, R. J. Hoffman, R. C. Winterton, *J. Electrochem. Soc.* **1990**, *137*, 775.

[14] O. Mizrahi, N. Amir, E. Pollak, O. Chusid, V. Marks, H. Gottlieb, L. Larush, E. Zinigrad, D. Aurbach, *J. Electrochem. Soc.* **2008**, *155*, A103.

[15] D. Aurbach, G. S. Suresh, E. Levi, A. Mitelman, O. Mizrahi, O. Chusid, M. Brunelli, *Adv. Mater.* **2007**, *19*, 4260.

[16] a) Y. Vestfried, O. Chusid, Y. Goffer, P. Aped, D. Aurbach, *Organometallics* **2007**, *26*, 3130; b) N. Pour, Y. Gofer, D. T. Major, D. Aurbach, *J. Am. Chem. Soc.* **2011**, *133*, 6270.

[17] C. Liebenow, Z. Yang, P. Lobitz, *Electrochem. Commun.* **2000**, *2*, 641.

[18] H. S. Kim, T. S. Arthur, G. D. Allred, J. Zajicek, J. G. Newman, A. E. Rodnyansky, A. G. Oliver, W. C. Boggess, J. Muldoon, *Nat. Commun.* **2011**, *2*, 427.

[19] a) Z. Zhao-Karger, X. Zhao, D. Wang, T. Diemant, R. J. Behm, M. Fichtner, *Adv. Energy Mater.* **2015**, *5*, 1401155; b) Z. Zhao-Karger, X. Zhao, O. Fuhr, M. Fichtner, *RSC Adv.* **2013**, *3*, 16330.

[20] C. Liao, N. Sa, B. Key, A. K. Burrell, L. Cheng, L. A. Curtiss, J. T. Vaughey, J.-J. Woo, L. Hu, B. Pan, Z. Zhang, *J. Mater. Chem. A.* **2015**, *3*, 6082.

[21] F.-F. Wang, Y.-S. Guo, J. Yang, Y. Nuli, S.-I. Hirano, *Chem. Commun.* **2012**, *48*, 10763.

[22] E. G. Nelson, J. W. Kampf, B. M. Bartlett, *Chem. Commun.* **2014**, *50*, 5193.

[23] P. Bian, Y. NuLi, Z. Abudoureyimu, J. Yang, J. Wang, *Electrochim. Acta.* **2014**, *121*, 258.

[24] B. Pan, J. Zhang, J. Huang, J. T. Vaughey, L. Zhang, S.-D. Han, A. K. Burrell, Z. Zhang, C. Liao, *Chem. Commun.* **2015**, *51*, 6214.

[25] a) R. E. Doe, R. Han, J. Hwang, A. J. Gmitter, I. Shterenberg, H. D. Yoo, N. Pour, D. Aurbach, *Chem. Commun.* **2014**, *50*, 243; b) T. Liu, Y. Shao, G. Li, M. Gu, J. Hu, S. Xu, Z. Nie, X. Chen, C. Wang, J. Liu, *J. Mater. Chem. A.* **2014**, *2*, 3430; c) Z. Zhao-Karger, J. E. Mueller, X. Zhao, O. Fuhr, T. Jacob, M. Fichtner, *RSC Adv.* **2014**, *4*, 26924.

[26] a) O. Tutusaus, R. Mohtadi, T. S. Arthur, F. Mizuno, E. G. Nelson, Y. V. Sevryugina, *Angew. Chem., Int. Ed.* **2015**, *54*, 7900; b) R. Mohtadi, M. Matsui, T. S. Arthur, S.-J. Hwang, *Angew. Chem., Int. Ed.* **2012**, *51*, 9780.

[27] S. Y. Ha, Y. W. Lee, S. W. Woo, B. Koo, J. S. Kim, J. Cho, K. T. Lee, N. S. Choi, *ACS Appl. Mater. Interfaces* **2014**, *6*, 4063.

[28] Z. Ma, M. Kar, C. Xiao, M. Forsyth, D. R. MacFarlane, *Electrochem. Commun.* **2017**, *78*, 29.

[29] a) Z. Zhao-Karger, R. Liu, W. Dai, Z. Li, T. Diemant, B. P. Vinayan, C. Bonatto Minella, X. Yu, A. Manthiram, R. J. Behm, M. Ruben, M. Fichtner, *ACS Energy Lett.* **2018**, *3*, 2005; b) Z. Zhao-Karger, M. E. G. Bardaji, O. Fuhr, M. Fichtner, *J. Mater. Chem. A.* **2017**, *5*, 10815.

[30] T. Mandai, Y. Youn, Y. Tateyama, *Mater. Adv.* **2021**, *2*, 6283.

[31] J. Luo, Y. Bi, L. Zhang, X. Zhang, T. L. Liu, *Angew. Chem., Int. Ed.* **2019**, *58*, 6967.

[32] a) L. P. Wang, Z. Y. Li, Z. Meng, Y. L. Xiu, B. Dasari, Z. Zhao-Karger, M. Fichtner, *Energy Storage Mater.* **2022**, *48*, 155; b) X. Ge, F. Song, A. Du, G. Sun, S. Zhang, J. Zhao, Q. Zhang, X. Zhou, B. Zhang, G. Cui, *ACS Energy Lett.* **2023**, *8*, 3685; c) A. Du, H. Zhang, Z. Zhang, J. Zhao, Z. Cui, Y. Zhao, S. Dong, L. Wang, X. Zhou, G. Cui, *Adv. Mater.* **2019**, *31*, 1805930; d) L. C. Merrill, H. O. Ford, J. L. Schaefer, *ACS Appl. Energy Mater.* **2019**, *2*, 6355; e) P. Wang, J. Trück, J. Häcker, A. Schlosser, K. Küster, U. Starke, L. Reinders, M. R. Buchmeiser, *Energy Storage Mater.* **2022**, *49*, 509; f) L. Wang, S. Riedel, A. Welle, S. Vincent, S. Dinda, B. Dasari, J. M. Garcia Lastra, B. Esser, Z. Zhao-Karger, *ACS Appl. Energy Mater.* **2024**, *7*, 5857.

[33] a) X. S. Ge, F. C. Song, A. B. Du, Y. J. Zhang, B. Xie, L. Huang, J. W. Zhao, S. M. Dong, X. H. Zhou, G. L. Cui, *Adv. Energy Mater.* **2022**, *12*, 2201464; b) Y. Shao, N. N. Rajput, J. Hu, M. Hu, T. Liu, Z. Wei, M. Gu, X. Deng, S. Xu, K. S. Han, J. Wang, Z. Nie, G. Li, K. R. Zavadil, J. Xiao, C. Wang, W. A. Henderson, J.-G. Zhang, Y. Wang, K. T. Mueller, K. Persson, J. Liu, *Nano Energy* **2015**, *12*, 750.

[34] Z. X. Wei, D. K. Singh, K. Helmbrecht, J. Sann, Y. Yusim, J. A. Kieser, C. Glaser, M. Rohnke, A. Gross, J. Janek, *Adv. Energy Mater.* **2023**, *13*, 2302525.

[35] a) R. L.e Ruyet, B. Fleutot, R. Berthelot, Y. Benabed, G. Hautier, Y. Filinchuk, R. Janot, *ACS Appl. Energy Mater.* **2020**, *3*, 6093; b) S. Higashi, K. Miwa, M. Aoki, K. Takechi, *Chem. Commun.* **2014**, *50*, 1320; c) C. Glaser, Z. Wei, S. Indris, P. Klement, S. Chatterjee, H. Ehrenberg, Z. Zhao-Karger, M. Rohnke, J. Janek, *Adv. Energy Mater.* **2023**, *13*, 2301980; d) L.-P. Wang, Z. Zhao-Karger, F. Klein, J. Chable, T. Braun, A. R. Schür, C.-R. Wang, Y.-G. Guo, M. Fichtner, *ChemSusChem* **2019**, *12*, 2286.

[36] P. Canepa, S.-H. Bo, G. Sai Gautam, B. Key, W. D. Richards, T. Shi, Y. Tian, Y. Wang, J. Li, G. Ceder, *Nat. Commun.* **2017**, *8*, 1759.

[37] W. Zhao, Z. Pan, Y. Zhang, Y. Liu, H. Dou, Y. Shi, Z. Zuo, B. Zhang, J. Chen, X. Zhao, X. Yang, *Angew. Chem., Int. Ed.* **2022**, *61*, 202205187.

[38] C. Li, R. D. Guha, A. Shyamsunder, K. A. Persson, L. F. Nazar, *Energy Environ. Sci.* **2024**, *17*, 190.

[39] Y. Sun, Y. Wang, L. Jiang, D. Dong, W. Wang, J. Fan, Y.-C. Lu, *Energy Environ. Sci.* **2023**, *16*, 265.

[40] Y. Du, Y. Chen, S. Tan, J. Chen, X. Huang, L. Cui, J. Long, Z. Wang, X. Yao, B. Shang, G. Huang, X. Zhou, L. Li, J. Wang, F. Pan, *Energy Storage Mater.* **2023**, *62*, 102939.
[41] N. T. Hahn, T. J. Seguin, K.-C. Lau, C. Liao, B. J. Ingram, K. A. Persson, K. R. Zavadil, *J. Am. Chem. Soc.* **2018**, *140*, 11076.
[42] H. Dong, O. Tutusaus, Y. Liang, Y. Zhang, Z. Lebens-Higgins, W. Yang, R. Mohtadi, Y. Yao, *Nat. Energy* **2020**, *5*, 1043.
[43] Z. Zhao-Karger, R. Liu, W. Dai, Z. Li, T. Diemant, B. P. Vinayan, C. Bonatto Minella, X. Yu, A. Manthiram, R. J. Behm, M. Ruben, M. Fichtner, *ACS Energy Lett.* **2018**, *3*, 2005.
[44] D. Aurbach, R. Skaletsky, Y. Gofer, *J. Electrochem. Soc.* **1991**, *138*, 3536.
[45] K. A. See, J. A. Gerbec, Y.-S. Jun, F. Wudl, G. D. Stucky, R. Seshadri, *Adv. Energy Mater.* **2013**, *3*, 1056.
[46] A. Ponrouch, C. Frontera, F. Bardé, M. R. Palacín, *Nat. Mater.* **2016**, *15*, 169.
[47] D. Wang, X. Gao, Y. Chen, L. Jin, C. Kuss, P. G. Bruce, *Nat. Mater.* **2018**, *17*, 16.
[48] M. Wang, C. Jiang, S. Zhang, X. Song, Y. Tang, H.-M. Cheng, *Nat. Chem.* **2018**, *10*, 667.
[49] a) Z. Li, O. Fuhr, M. Fichtner, Z. Zhao-Karger, *Energy Environ. Sci.* **2019**, *12*, 3496; b) A. Shyamsunder, L. E. Blanc, A. Assoud, L. F. Nazar, *ACS Energy Lett.* **2019**, *4*, 2271.
[50] Z. Zhao-Karger, Y. Xiu, Z. Li, A. Reupert, T. Smok, M. Fichtner, *Nat. Commun.* **2022**, *13*, 3849.
[51] S. Biria, S. Pathreeker, H. Li, I. D. Hosein, *ACS Appl. Energy Mater.* **2019**, *2*, 7738.
[52] J. Forero-Saboya, C. Bodin, A. Ponrouch, *Electrochem. Commun.* **2021**, *124*, 106936.
[53] R. Zhou, Z. Hou, Q. Liu, X. Du, J. Huang, B. Zhang, *Adv. Funct. Mater.* **2022**, *32*, 2200929.
[54] Z. Hou, R. Zhou, Z. Min, Z. Lu, B. Zhang, *ACS Energy Lett.* **2022**, *8*, 274.
[55] K. V. Nielson, J. Luo, T. L. Liu, *Batteries Supercaps* **2020**, *3*, 766.
[56] S. Kim, N. T. Hahn, T. T. Fister, N. J. Leon, X.-M. Lin, H. Park, P. Zapol, S. H. Lapidus, C. Liao, J. T. Vaughey, *Chem. Mater.* **2023**, *35*, 2363.
[57] N. J. Leon, X. Xie, M. Yang, D. M. Driscoll, J. G. Connell, S. Kim, T. Seguin, J. T. Vaughey, M. Balasubramanian, K. A. Persson, C. Liao, *J. Phys. Chem. C.* **2022**, *126*, 13579.
[58] K. Kisu, S. Kim, T. Shinohara, K. Zhao, A. Züttel, S.-I. Orimo, *Sci. Rep.* **2021**, *11*, 7563.
[59] A. T. Landers, J. Self, S. A. McClary, K. J. Fritzsching, K. A. Persson, N. T. Hahn, K. R. Zavadil, *J. Phys. Chem. C.* **2023**, *127*, 23664.
[60] S. Biria, S. Pathreeker, F. S. Genier, F.-H. Chen, H. Li, C. V. Burdin, I. D. Hosein, *ACS Omega* **2021**, *6*, 17095.
[61] S. Biria, S. Pathreeker, F. S. Genier, I. D. Hosein, *ACS Appl. Polym. Mater.* **2020**, *2*, 2111.
[62] K. Xu, *Chem. Rev.* **2014**, *114*, 11503.
[63] J.-F. Ding, R. Xu, C. Yan, B.-Q. Li, H. Yuan, J.-Q. Huang, *J. Energy Chem.* **2021**, *59*, 306.
[64] N. Amir, Y. Vestfrid, O. Chusid, Y. Gofer, D. Aurbach, *J. Power Sources* **2007**, *174*, 1234.
[65] a) Y. Zhao, A. Wang, L. Ren, X. Liu, J. Luo, *J. Energy Chem.* **2022**, *70*, 174; b) X.-B. Cheng, R. Zhang, C.-Z. Zhao, Q. Zhang, *Chem. Rev.* **2017**, *117*, 10403.
[66] Z. Li, X. Mu, Z. Zhao-Karger, T. Diemant, R. J. Behm, C. Kubel, M. Fichtner, *Nat. Commun.* **2018**, *9*, 5115.
[67] D. S. Tchitchekova, D. Monti, P. Johansson, F. Bardé, A. Randon-Vitanova, M. R. Palacín, A. Ponrouch, *J. Electrochem. Soc.* **2017**, *164*, A1384.
[68] a) T. J. Seguin, N. T. Hahn, K. R. Zavadil, K. A. Persson, *Front. Chem.* **2019**, *7*, 175; b) N. N. Rajput, X. Qu, N. Sa, A. K. Burrell, K. A. Persson, *J. Am. Chem. Soc.* **2015**, *137*, 3411.
[69] M. Salama, I. Shterenberg, H. Gizbar, N. N. Eliaz, M. Kosa, K. Keinan-Adamsky, M. Afri, L. J. W. Shimon, H. E. Gottlieb, D. T. Major, Y. Gofer, D. Aurbach, *J. Phys. Chem. C.* **2016**, *120*, 19586.
[70] D. Zhang, S. Duan, X. Liu, Y. Yang, Y. Zhang, W. Ren, S. Zhang, M. Cheng, W. Yang, J. Wang, Y. NuLi, *Nano Energy* **2023**, *109*, 108257.
[71] a) M. Salama, I. Shterenberg, L. J. W. Shimon, K. Keinan-Adamsky, M. Afri, Y. Gofer, D. Aurbach, *J. Phys. Chem. C.* **2017**, *121*, 24909; b) I. Shterenberg, M. Salama, H. D. Yoo, Y. Gofer, J.-B. Park, Y.-K. Sun, D. Aurbach, *J. Electrochem. Soc.* **2015**, *162*, A7118.
[72] a) S.-B. Son, T. Gao, S. P. Harvey, K. X. Steirer, A. Stokes, A. Norman, C. Wang, A. Cresce, K. Xu, C. Ban, *Nat. Chem.* **2018**, *10*, 532; b) Y. Zhao, A. Du, S. Dong, F. Jiang, Z. Guo, X. Ge, X. Qu, X. Zhou, G. Cui, *ACS Energy Lett.* **2021**, *6*, 2594; c) R. Zhang, C. Cui, R. Li, Y. Li, C. Du, Y. Gao, H. Huo, Y. Ma, P. Zuo, G. Yin, *Chem. Eng. J.* **2021**, *426*, 130751; d) S. Shin, J. H. Kwak, S. H. Oh, H.-S. Kim, S.-H. Yu, H.-D. Lim, *ACS Appl. Mater. Interfaces* **2023**, *15*, 28684; e) Z. Meng, Z. Li, L. Wang, T. Diemant, D. Bosubabu, Y. Tang, R. Berthelot, Z. Zhao-Karger, M. Fichtner, *ACS Appl. Mater. Interfaces* **2021**, *13*, 37044.
[73] X. Huang, S. Tan, J. Chen, Z. Que, R. Deng, J. Long, F. Xiong, G. Huang, X. Zhou, L. Li, J. Wang, L. Mai, F. Pan, *Adv. Funct. Mater.* **2024**, *34*, 2314146.
[74] a) M. Wang, W. Sun, K. Zhang, Z. Zhang, A. Du, S. Dong, J. Zhang, J. Liu, X. Chen, Z. Zhou, F. Li, Z. Li, G. Li, G. Cui, *Energy Environ. Sci.* **2024**, *17*, 630; b) F. Wang, H. Hua, D. Wu, J. Li, Y. Xu, X. Nie, Y. Zhuang, J. Zeng, J. Zhao, *ACS Energy Lett.* **2022**, *8*, 780; c) Z. Li, D.-T. Nguyen, J. D. Bazak, K. S. Han, Y. Chen, V. Prabhakaran, T. T. Le, Z. Cheng, M. Song, V. G. Pol, K. T. Mueller, V. Murugesan, *Adv. Energy Mater.* **2024**, *14*, 2301544; d) Y. Liu, W. Zhao, Z. Pan, Z. Fan, M. Zhang, X. Zhao, J. Chen, X. Yang, *Angew. Chem., Int. Ed. Engl.* **2023**, *62*, 202302617.
[75] a) B. Pan, J. Huang, N. Sa, S. M. Brombosz, J. T. Vaughey, L. Zhang, A. K. Burrell, Z. Zhang, C. Liao, *J. Electrochem. Soc.* **2016**, *163*, A1672; b) H. Dong, Y. Liang, O. Tutusaus, R. Mohtadi, Y. Zhang, F. Hao, Y. Yao, *Joule* **2019**, *3*, 782.
[76] G. Yang, Y. Li, J. Wang, Y. Lum, C. Y. J. Lim, M.-F. Ng, C. Zhang, Z. Chang, Z. Zhang, A. D. Handoko, T. Ghosh, S. Li, Z. Sofer, W. Liu, Y. Yao, Z. W. Seh, *Energy Environ. Sci.* **2024**, *17*, 1141.
[77] X. Li, T. Gao, F. Han, Z. Ma, X. Fan, S. Hou, N. Eidson, W. Li, C. Wang, *Adv. Energy Mater.* **2017**, *8*, 1701728.
[78] D. Chinnadurai, W. Y. Lieu, S. Kumar, G. Yang, Y. Li, Z. W. Seh, *Nano Lett.* **2023**, *23*, 1564.
[79] A. Roy, V. B. Parambath, T. Diemant, G. Neusser, C. Kranz, R. J. Behm, Z. Y. Li, Z. Zhao-Karger, M. Fichtner, *Batteries Supercaps* **2022**, *5*, 202100305.
[80] B. Li, R. Masse, C. Liu, Y. Hu, W. Li, G. Zhang, G. Cao, *Energy Storage Mater.* **2019**, *22*, 96.
[81] S. Y. Li, J. H. Zhang, S. C. Zhang, Q. L. Liu, H. Cheng, L. Fan, W. D. Zhang, X. Y. Wang, Q. Wu, Y. Y. Lu, *Nat. Energy* **2024**, *9*, 285.
[82] N. Singh, T. S. Arthur, O. Tutusaus, J. Li, K. Kisslinger, H. L. Xin, E. A. Stach, X. Fan, R. Mohtadi, *ACS Appl. Energy Mater.* **2018**, *1*, 4651.
[83] J. Forero-Saboya, C. Davoisne, R. Dedryvère, I. Yousef, P. Canepa, A. Ponrouch, *Energy Environ. Sci.* **2020**, *13*, 3423.
[84] K. Ta, R. Zhang, M. Shin, R. T. Rooney, E. K. Neumann, A. A. Gewirth, *ACS Appl. Mater. Interfaces* **2019**, *11*, 21536.
[85] Y. Jie, Y. Tan, L. Li, Y. Han, S. Xu, Z. Zhao, R. Cao, X. Ren, F. Huang, Z. Lei, G. Tao, G. Zhang, S. Jiao, *Angew. Chem., Int. Ed.* **2020**, *59*, 12689.
[86] S. A. McClary, D. M. Long, A. Sanz-Matias, P. G. Kotula, D. Prendergast, K. L. Jungjohann, K. R. Zavadil, *ACS Energy Lett.* **2022**, *7*, 2792.
[87] Z. Yang, N. J. Leon, C. Liao, B. J. Ingram, L. Trahey, *ACS Appl. Mater. Interfaces* **2023**, *15*, 25018.
[88] a) X. Xie, N. J. Leon, D. W. Small, E. W. C. Spotte-Smith, C. Liao, K. A. Persson, *J. Phys. Chem. C.* **2022**, *126*, 20773; b) T. Pavčnik, J. D. Forero-Saboya, A. Ponrouch, A. Robba, R. Dominko, J. Bitenc, *J. Mater. Chem. A.* **2023**, *11*, 14738.

Liping Wang is currently a research scientist at Ulm University. She received Ph.D. in physical chemistry from the University of Chinese Academy of Sciences in 2019, during which she spent one year as a visiting scholar at the Helmholtz Institute Ulm for Electrochemical Energy Storage (HIU). From 2019 to 2022, she worked as a research scientist at Karlsruhe Institute of Technology (KIT). Subsequently, she joined Ulm University funded by The Cluster of Excellence POLiS, where her research focuses on post-lithium batteries, specifically magnesium- and calcium-based systems. Her project involves the development of novel electrolytes and sulfur cathodes.

Sibylle Riedel is a postdoctoral researcher for advanced battery materials at the Helmholtz-Institute Ulm for Electrochemical Energy Storage (HIU) and Karlsruhe Institute of Technology (KIT) funded by the German Cluster of Excellence POLiS ("Energy Storage Beyond Lithium"). She received her Ph.D. in organic chemistry at the University of Tübingen and joined HIU and KIT 2021 with a focus on post-lithium batteries, specifically magnesium- and calcium-based systems. Her project involves the development of novel electrolytes and organic cathodes.

Zhirong Zhao-Karger is a research group leader for advanced battery materials at the Institute of Nanotechnology (INT) of the Karlsruhe Institute of Technology (KIT). She received her Ph.D. in organic chemistry at the University Hannover, Germany. After the postdoctoral research at the Catalysis Research Laboratory of the University of Heidelberg, she joined the INT as a research scientist in 2008 and has been working in the field of electrochemical energy storage since 2013 with a focus on post-lithium batteries, such as magnesium and calcium-based systems.